Electron Cloud in Wigglers

F. Zimmermann, D. Schulte*,

C. Vaccarezza, M. Zobov†,

R. Wanzenberg‡

December 18, 2005

Abstract

Substantial electron densities may accrue inside the wigglers of future linear-collider damping rings, since the wiggler photon flux can only partially be absorbed by antechambers. In an operating positron ring, at DAFNE, a fast instability with electron-cloud signature has indeed been observed after modifications to the wiggler field. Simulations of electron-cloud build up in wigglers allow us to explore the dependence of the electron density and decay time on the magnet and beam parameters. Without additional countermeasures, the simulated electron densities easily exceed the thresholds of electron-driven single and multi-bunch instabilities. The latter are modelled by separate computer programmes. In this report, simulations of electron build up and instabilities are presented for the damping rings of ILC and CLIC, as well as for DAFNE.

*CERN, Geneva, Switzerland
†INFN, Frascati, Italy
‡DESY, Hamburg, Germany

1 Introduction

Based on the experience at KEKB and PEP-II, the electron cloud has been identified as a major potential threat to achieving design performance at future linear-collider damping rings. Of particular concern is the electron cloud in the wiggler sections, since the wigglers (1) occupy a large fraction of the collider ring, (2) experience the largest flux of photons, thereby constituting an ample source of photo-electrons, and (3) exhibit a complex magnetic field pattern, which could trap electrons for a long time or lead to enhanced multipacting. It is interesting that the DAFNE positron ring experiences a horizontal instability which shows characters of an electron-cloud driven effect. This instability presently limits the maximum positron beam current which can be stored. In previous years, until 2002, no such instability and related current limit were noticed (if the instability existed at the time, it was masked by beam-beam effects). With a fill pattern of 45–50 bunches separated by empty buckets a beam current of 1.2 A was reached in 2002, while presently only 0.4–0.5 A can be stored in the same fill pattern of 2002. Therefore, in 2004/2005, a total of 100–110 bunches are injected into successive buckets, in which condition a current of 1.4 A is achieved. One of the major changes in 2003 was a smoothing of the nonlinear wiggler field. If the interpretation of an electron-cloud effect in the DAFNE wigglers is confirmed, DAFNE could serve as a crucial experimental testbed for the modeling of electron-cloud behavior in wigglers.
This report aims to review the present understanding and recent studies of electron-cloud phenomena for wigglers. In the following section, we present and compare the pertinent parameters for TESLA/ILC, CLIC, and DAFNE. We next describe the results of photon-flux simulations, before discussing the simulated electron densities for various ILC/TESLA and CLIC wiggler models. Then, we briefly explore single-bunch instability thresholds at the two linear-collider damping rings. The subsequent section is devoted to the observations at, and simulations for, DAFNE. Finally, we will draw some conclusions.

2 Parameters

Table 1 compiles relevant beam and wiggler parameters for the ILC/TESLA damping ring, the CLIC damping ring and DAFNE. Many parameters, e.g., the wiggler field or the beam line density, are remarkably similar for all three projects. Noteworthy differences are the total lengths of the wiggler sections, ranging from 8 m in DAFNE to 540 m at the ILC, and the vertical beam sizes, decreasing from 80 μm in DAFNE to a few microns for the linear-collider rings.
An important ingredient of the electron build-up simulations is the number of photo-electrons emitted per positron and per meter. It is obtained by multiplying the simulated photon flux incident outside the wiggler antechamber with a typical photo-emission yield $Y \approx 0.1$ [1], for ILC and CLIC, and with $Y \approx 0.2$ for DAFNE. The latter is the photo-emission yield measured for the DAFNE aluminium vacuum chamber [2]. The photon-flux simulations for ILC and CLIC were performed using the code PHOTON [3]. Those for DAFNE, showing a much smaller flux outside the antechamber, were done

by C. Vaccarezza and colleagues from the Frascati team [4]. In Table 1, the DAFNE parameters from 2002, i.e., for the operating conditions prior to the wiggler modification, are shown in parentheses.

Table 1: Wiggler and Beam Parameters

parameter	symbol	TESLA/ILC	CLIC	DAFNE
energy	E	5 GeV	2.4242 GeV	0.510 GeV
circumference	C	17 km	357 m	97.69 m
wiggler length	$l_{w,tot}$	540 m	160 m	8 m
energy loss per turn	U_0	20 MeV	2.19 MeV	9.2 keV
damping time	τ_s	28 ms	2.62 ms	18 ms
wiggler bending radius	ρ_w	9.9 m	4.58 m	1.0 m
wiggler bending field	B_w	1.63 T	1.76 T	1.7 T
wiggler period	λ_w	0.40 m	0.20 m	0.65 m
wiggler h. beta function	β_{xw}	10.5 m	4.0 m	3.4 (2.4) m
wiggler v. beta function	β_{yw}	10.5 m	7.0 m	1.1 (1.1) m
hor. emittance at inj.	$\epsilon_{x,inj}$	1 μm	13 nm	N/A
vert. emittance at inj.	$\epsilon_{y,inj}$	1 μm	320 pm	N/A
hor. emittance at extr.	$\epsilon_{x,ext}$	818 pm	131 pm	0.42 (0.76) μm
vert. emittance at extr.	$\epsilon_{y,ext}$	2 pm	2 pm	1.3 (2.3) nm
final hor. beam size	σ_{xw}	93 μm	22.8 μm	1.3 (1.4) mm
final vert. beam size	σ_{xw}	5 μm	3.6 μm	0.04 (0.05) mm
bunch population	N_b	2×10^{10}	4.2×10^9	2.1×10^{10} (4.3×10^{10})
bunch length	σ_z	6 mm	1.3 mm	17 (22) mm
bunch spacing	$L_{\rm sep}$	6 m	0.2 m	0.8 (1.6) m
aperture half width in wiggler	h_x	16 mm	16 mm	60 mm
aperture half height in wiggler	h_y	9 mm	9 mm	10 mm
beam line density	λ_b	3.3×10^9 m^{-1}	2.1×10^{10} m^{-1}	2.6×10^{10} m^{-1}
photon rate / e^+ & m	dN_γ/dz	10.4 m^{-1}	10.9 m^{-1}	10.5 m^{-1}
photo-el. rate / e^+ & m	dN_{pe}/dz	0.1 m^{-1}	0.3 m^{-1}	0.018 m^{-1}

3 Photon Distributions

For TESLA/ILC and CLIC a number of Monte-Carlo simulations were performed, in order to determine the incident photon distribution. The model of the TESLA or CLIC wiggler vacuum chamber considered in these simulations is shown in Fig. 1 [1]. The horizontal and vertical half apertures of the beam-pipe proper are 16 and 9 mm, respectively. The half height of the antechamber slots is 3 mm. In photon-flux simulations, the photons incident at $|y| < 3$ mm are assumed to be absorbed by the antechamber.

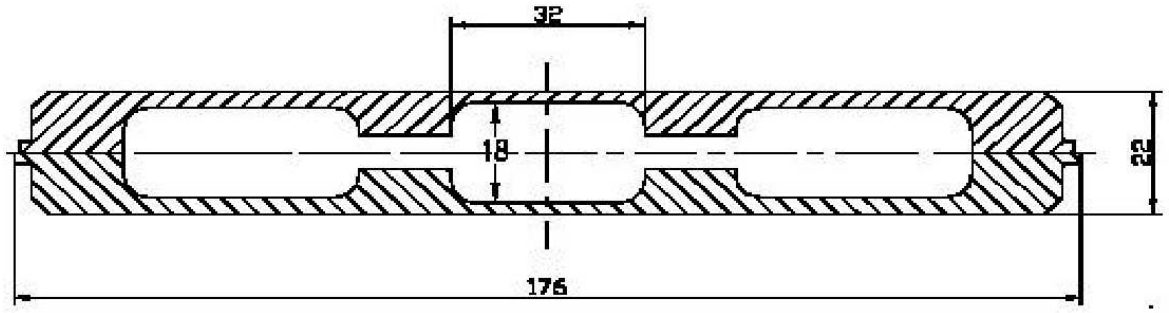

Figure 1: Model for vacuum chamber in TESLA/ILC or CLIC wiggler. The full height of the antechamber slot is taken to be 6 mm.

Figures 2 and 3 present the simulated photon flux on the wall per meter length as a function of longitudinal position for the TESLA/ILC and CLIC damping ring, respectively. Photons hitting the pipe wall anywhere around the ring at a vertical position of less than 3 mm are taken to enter into a perfectly absorbing antechamber, while photons hitting at larger vertical amplitudes are assumed to be specularly reflected with a probability of 80%. Only the contributions of photons lost on the beam pipe proper are included in these and the following figures. The flux incident inside the wigglers is about 2×10^{18} photons per meter and per second for TESLA/ILC and about 3×10^{18} photons per meter and per second for CLIC. Figures 2 and 3 refer to the beam emittances at injection. For the beam emittances at extraction (results not shown here, but published in [1]), the flux in TESLA reduces by about an order of magnitude, while that in CLIC, with lower injected beam emittances, decreases by only about 10% [1]. It is interesting to remark that for the ILC the photon flux incident on the chamber proper is non-zero everywhere around the ring, while for the LHC the arc antechamber efficiently absorbs all photons.
Figures 4 and 5 show the flux converted to an average number of incident photons per passing positron and per meter length in case of TESLA/ILC and CLIC, respectively, again for the injection conditions. We find that for the wiggler of TESLA/ILC about 1 photon hits the beam pipe proper per passing positron per meter, while for the CLIC wiggler about 3 photons impact the central vacuum chamber per meter. The TESLA/ILC number decreases to 0.1 photons per positron and meter for the final beam emittances, while the CLIC number barely changes.
The average energy of the photons incident on the beam-pipe wall is displayed in Figs. 6 and 7. The average photon energies are about 4 keV in the TESLA/ILC wiggler and 2.2 keV in the CLIC wiggler.
The following two figures, Figs. 8 and 9, show the heat load resulting from photons which are absorbed by the beam pipe proper. In the wiggler, the maximum heat load is about 2 kW/m for TESLA/ILC and 9 kW/m for CLIC. This amount of heat could pose a problem for common wiggler-magnet technologies. It indicates a need for dedicated reduced-aperture photon absorbers in addition to the antechamber.

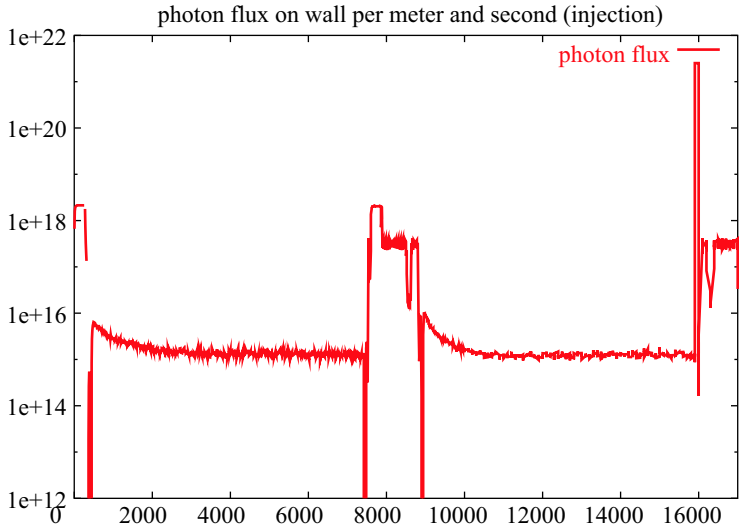

Figure 2: Photon flux on the wall per meter at injection into the TESLA/ILC damping ring [1], computed by PHOTON [3]. Visible are the two 'short' wiggler sections with highest flux, at 0 and 8 km, which are preceded and followed, respectively, by arcs with a somewhat reduced photon flux. The lowest photon rates are seen in the long straight sections.

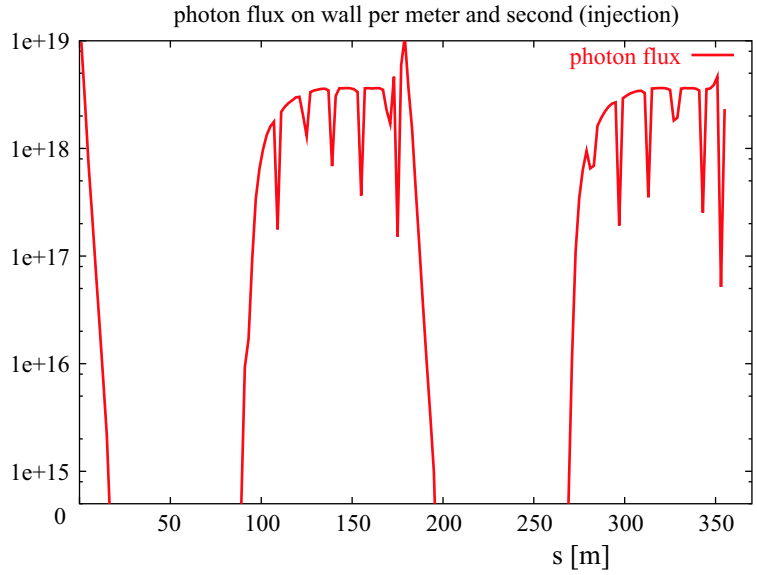

Figure 3: Photon flux on the wall per meter at injection into the CLIC damping ring [1], computed by PHOTON [3]. A significant photon flux occurs only in the wigglers, while in the arcs the antechambers efficiently absorb all of the radiation.

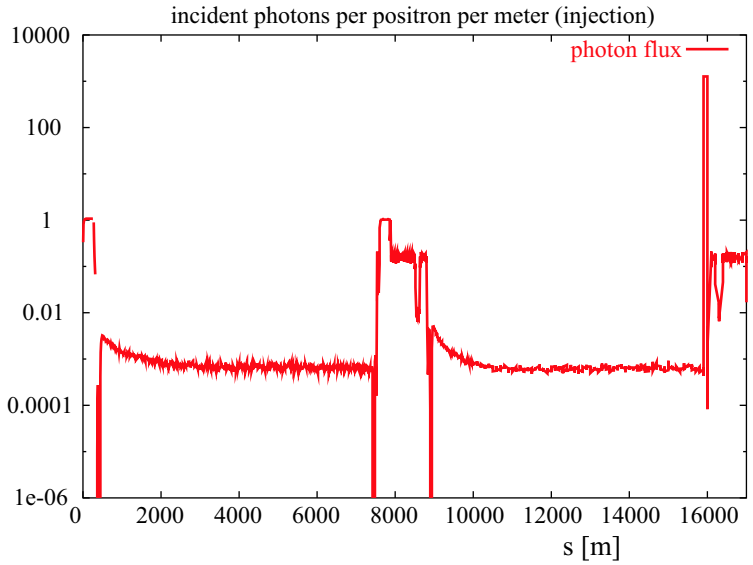

Figure 4: Photons incident on the wall of the TESLA/ILC damping ring per meter and per passing positron for beam parameters corresponding to injection [1], computed by PHOTON [3] (not counting photons absorbed in the antechamber).

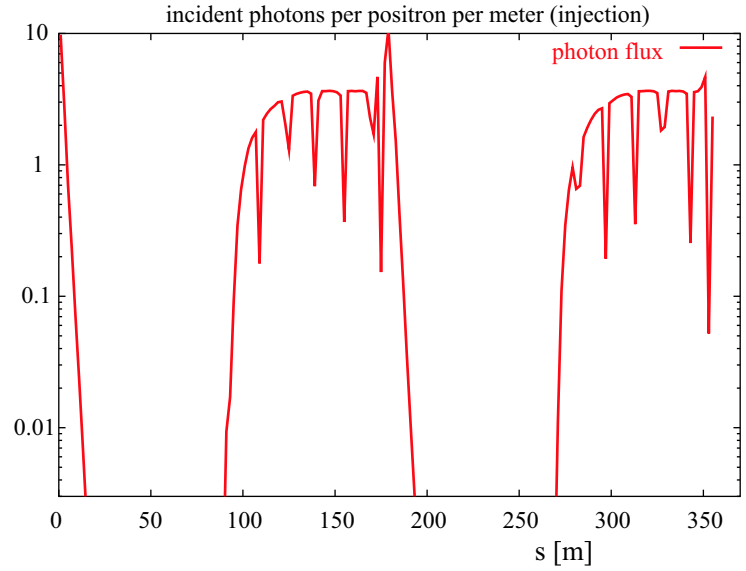

Figure 5: Photons incident on the wall of the CLIC damping ring per meter and per passing positron for beam parameters corresponding to injection [1], computed by PHOTON [3] (not counting photons absorbed in the antechamber).

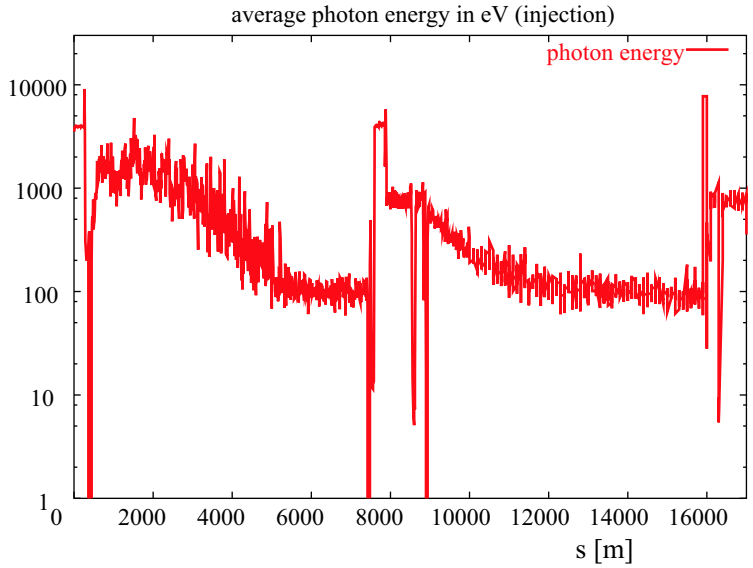

Figure 6: Average energy of photons (in eV) hitting the wall of the TESLA/ILC damping ring for beam parameters corresponding to injection (top) and extraction (bottom) [1], computed by PHOTON [3] (not counting photons absorbed in the antechamber).

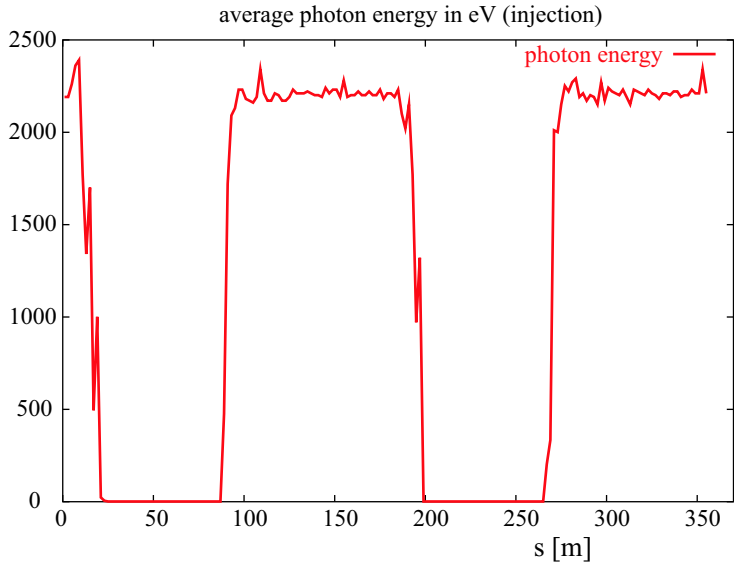

Figure 7: Average energy of photons (in eV) hitting the wall of the CLIC damping ring for beam parameters corresponding to injection (top) and extraction (bottom), computed by PHOTON [3] (not counting photons absorbed in the antechamber).

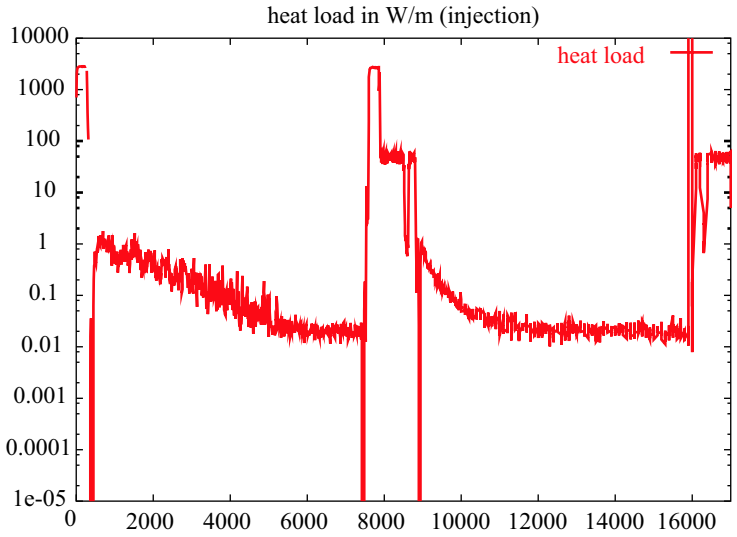

Figure 8: Synchrotron-radiation heat load on the wall of the TESLA/ILC damping ring for beam parameters corresponding to injection [1], computed by PHOTON [3] (photons absorbed in the antechamber were not counted).

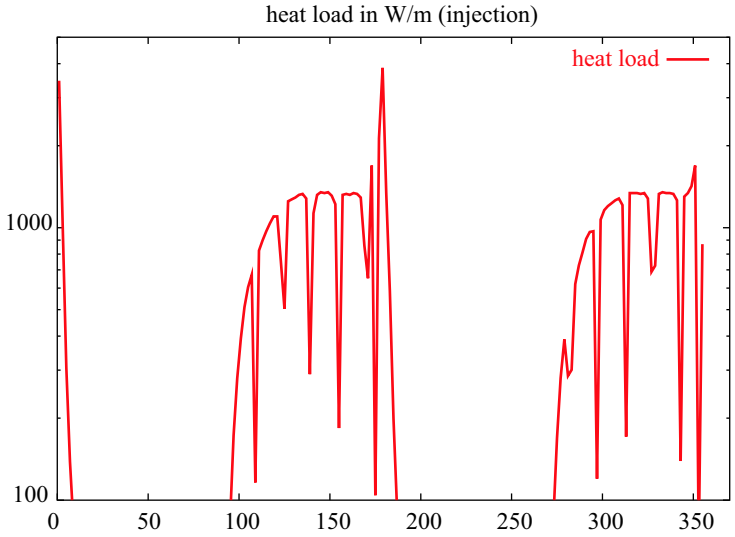

Figure 9: Synchrotron-radiation heat load on the wall of the CLIC damping ring for beam parameters corresponding to injection, computed by PHOTON [3] (photons absorbed in the antechamber were not counted).

4 Electron-Cloud Build Up

Simulations of the electron-cloud build up are performed with the ECLOUD code for different models of the wiggler field. The primary electron energy at which the maximum secondary emission yield assumes a maximum is chosen as $\epsilon_{\max} = 240$ eV for all cases. The elastic reflection probability in the limit of zero incident energy is taken to be 100%. As the simplest example, we consider a constant uniform dipole field equal to the peak wiggler field (1.68 T in case of TESLA). The line density simulated for the TESLA wiggler is shown in Fig. 10 and the central volume density in Fig. 11. The simulation assumed a primary photo-electron rate of 0.2 photo-electrons per meter per passing positron (two times larger than in Table 1), uniformly distributed in azimuth, and six different values of $\delta_{\max}$, ranging from 1.0 to 2.0 in steps of 0.2. The typical electron line density is of order 5×10^9 m^{-1} (comparable to the average beam line density of 3.3×10^9 m^{-1}), and the central volume density roughly 5×10^{12} m^{-3}. The electron build up saturates after about 100 ns and it shows a weak dependence on the secondary emission yield. The electron line density noticably increases only for a maximum secondary yield $\delta_{\max} \geq 1.8$.

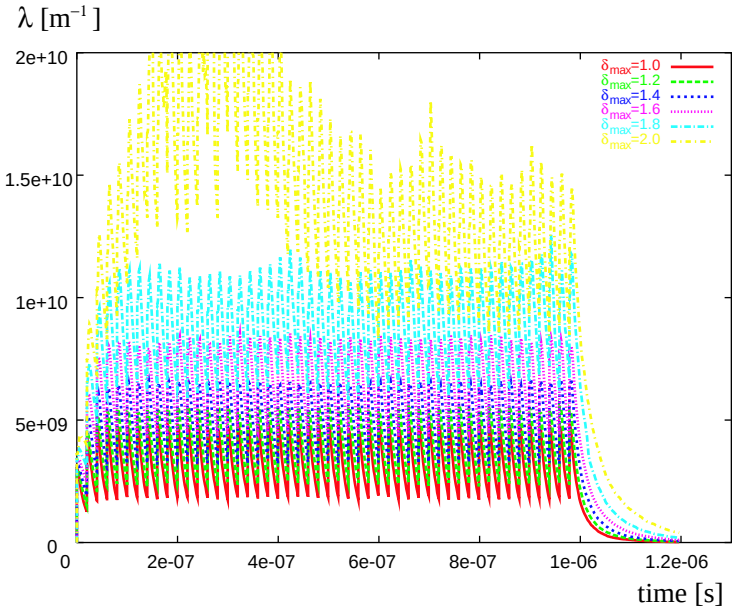

Figure 10: Electron line density in units of m^{-1} as a function of time in s for a bending field whose strength is equal to the peak field of the TESLA/ILC wiggler, assuming $dN_{e^-}/dz = 0.2$ photoelectrons per e$^+$ and meter; the various curves refer to six different values of $\delta_{\max}$.

The computer code ECLOUD [5] has been extended to handle also more sophisticated models of the magnetic field of a wiggler. For example, the wiggler field can be expanded in a cylindrical mode representation [6],

$$B_\rho \;=\; \sum A_{mn}\, I'_m(nk_z\rho)\, \sin(m\phi)\, \cos(nk_z z)\;, \qquad (1)$$

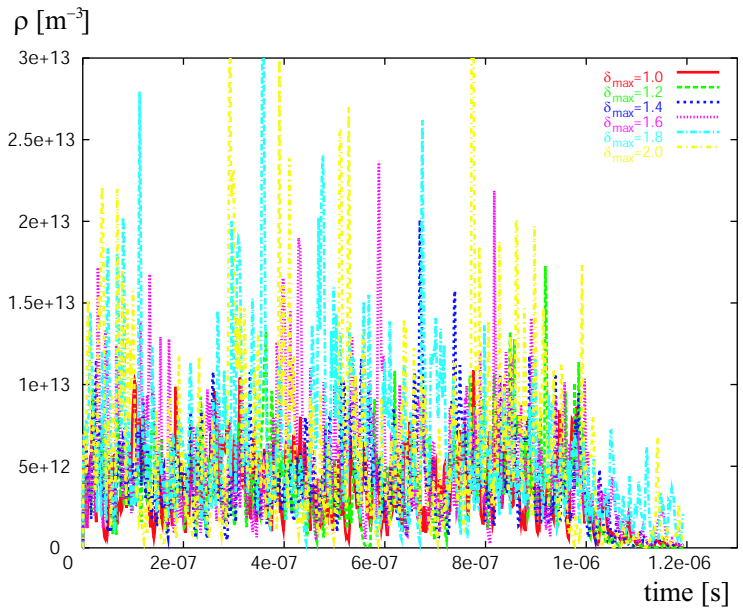

Figure 11: Central electron cloud volume density in units of m^{-3} as a function of time in s for a bending field whose strength is equal to the peak field of the TESLA wiggler, assuming $dN_{e^-}/dz = 0.2$ photoelectrons per e^+ and meter; the various curves refer to six different values of $\delta_{\max}$.

$$
\begin{aligned}
B_\phi &= \sum A_{mn} \frac{m}{nk_z\rho} I_m(nk_z\rho)\, \cos(m\phi)\, \cos(nk_z z)\ , \\
B_z &= -\sum A_{mn}\, I_m(nk_z\rho)\, \sin(m\phi)\, \sin(nk_z z)\ ,
\end{aligned}
$$

where $I_m(x)$ denotes the modified Bessel function of the first kind and A_{mn} are the expansions coefficients, which can be obtained from a Fourier analysis of the radial component of the wiggler field in the azimuthal and longitudinal variables at a fixed reference radius. Figures 12 and 13 show the simulated build up in the TESLA wiggler using a 1st order expansion of the wiggler field based on this cylindrical mode representation, keeping other parameters the same as above for the constant dipole field. The typical electron line and volume densities are again of order 5×10^9 m^{-1} and 5×10^{12} m^{-3}, respectively, i.e., the impact of the magnetic field variation appears to be small for TESLA/ILC.
An alternative model of a periodic magnet system, which is commonly used for planar wiggler magnets, is based on the following expansion in Cartesian coordinates (due to Halbach) :

$$
\begin{aligned}
B_y &= \sum_{n\,\mathrm{odd}} B_n\, \cosh(nk_y y)\, \sin(nk_z z) \qquad (2) \\
B_z &= \sum_{n\,\mathrm{odd}} B_n\, \sinh(nk_y y)\, \cos(nk_z z),
\end{aligned}
$$

with $k_y = k_z$. The results from the ECLOUD code for a 1st order expansion of the TESLA/ILC wiggler field in Cartesian coordinates are displayed in Figs. 14 and 15.

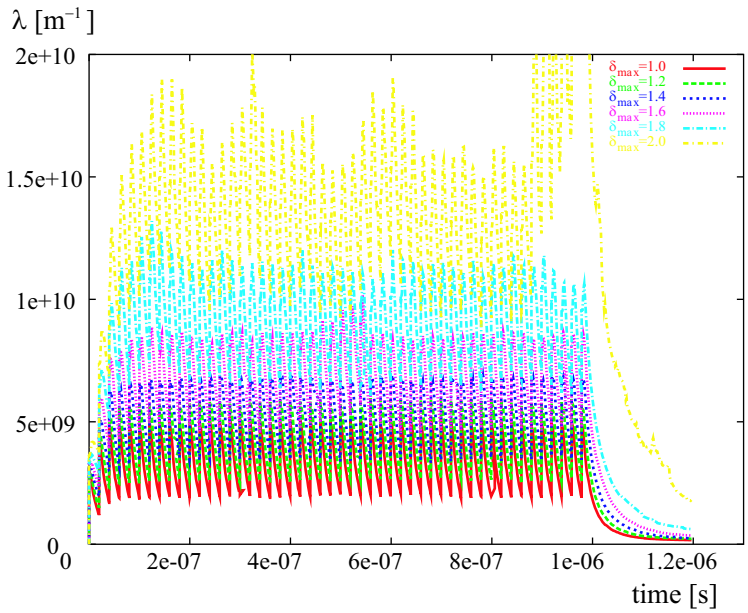

Figure 12: Electron line density in units of m^{-1} as a function of time in s for a 1st order expansion of the TESLA/ILC wiggler field in cylindrical coordinates, assuming $dN_{e^-}/dz = 0.2$ photoelectrons per e^+ and meter; the various curves refer to six different values of $\delta_{\max}$ [1].

The simulated line and volume densities are nearly indistinguishable from those obtained with the other two field models.

To reveal this similarity more explicitly, the simulated electron-line and central electron-cloud volume densities at $\delta_{\max} = 1.6$ are compared in Figs. 16 and 17 for the three different models of the wiggler field (i.e., constant bend, lowest-order cylindrical expansion, and harmonic expansion in Cartesian coordinates).

We conclude that for TESLA/ILC, the predicted electron cloud density does not strongly depend on the model of the wiggler field. This indicates that the longitudinal field component of the magnetic field of the TESLA/ILC wiggler does not change the dynamics of the electrons significantly. For a secondary emission yield of $\delta_{\max} = 1.6$ the simulations predict a central electron cloud volume density close to the average neutralization density, $N_b/(4h_x h_y L_{\rm sep}) \approx 6 \times 10^{12}$ m^{-3}.

A similar sequence of build-up simulations was also performed for CLIC. First, the magnetic field of the CLIC wiggler is modeled as a bend with a field strength equivalent to the peak magnetic field strength of the wiggler magnet (1.76 T). The simulated electron line and central electron-cloud volume densities are shown in Figs. 18 and 19, respectively. We here assumed a primary rate of either 0.0576 or 0.11 photo-electrons per passing positron per meter (six or three times lower than in Table 1, respectively), again uniformly distributed in azimuth. For moderate values of the maximum secondary emission yield, the line density is of order 5×10^9 m^{-1} (about a quarter of the beam line density $\sim 2 \times 10^{10}$ m^{-1} and roughly equal to the value found for ILC/TESLA), and the

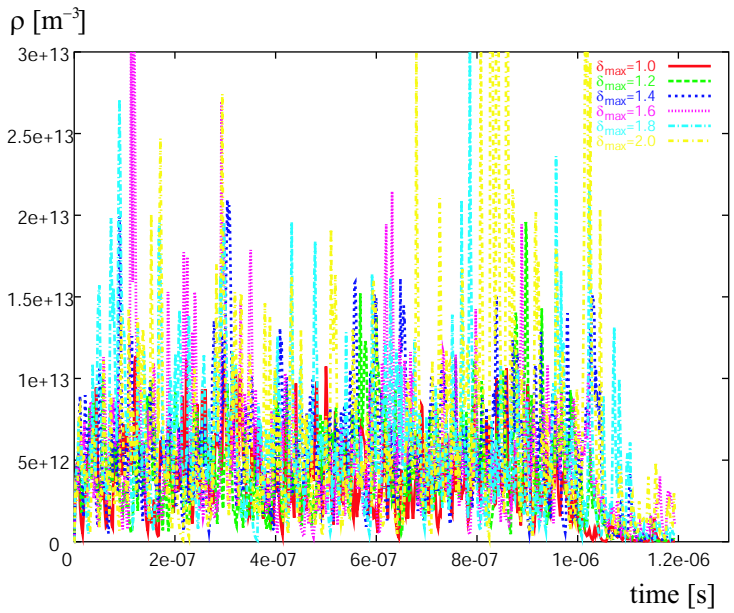

Figure 13: Central electron-cloud volume density in units of m^{-3} as a function of time in s for a 1st order expansion of the TESLA/ILC wiggler field in cylindrical coordinates, assuming $dN_{e^-}/dz = 0.2$ photoelectrons per e^+ and meter; the various curves refer to six different values of $\delta_{\max}$ [1].

central volume density for moderate $\delta_{\max}$ values is about $1 - 2 \times 10^{13}$ m^{-3}, or 2–4 times the ILC/TESLA number. The higher density at the center of the chamber, as compared with ILC/TESLA, indicates that electrons are trapped close to the beam during the passage of a bunch train. This is possible due to the much shorter bunch spacing and the lower charge per bunch in CLIC as compared with the ILC. The dependence on the secondary emission yield is more pronounced than for TESLA/ILC. The electron line density at CLIC noticably increases for a maximum secondary yield $\delta_{\max} \geq 1.2$ (as compared with a critical yield of about 1.8 for TESLA/ILC).

As for TESLA/ILC, also for CLIC the situation remains essentially unchanged in the case of the Cartesian wiggler field model. The simulation results for a 1st order harmonic expansion of the field in Cartesian coordinates are displayed in Figs. 20 and 21. Saturation is not yet reached after 35 ns, and the slope of the build up is again quite sensitive to the secondary emission yield. The typical line density at the end of the simulation of about 5×10^9 m^{-1} is similat to the value obtained before for the uniform field. The central volume density is also similar (compare Fig. 19). Small differences in the slope of the early build up are explained by the factor two difference in the assumed primary photo-electron rate and are not due to the difference in the magnetic field model.

Regardless of the observed insensitivity to the details of the field model, it is planned to upgrade the ECLOUD code so as to include realistic higher-order terms of the CLIC wiggler field. A promising approach in this direction is to apply the field description of Venturini [7], which appears to be the same as the one of Woodley and Wolski [6],

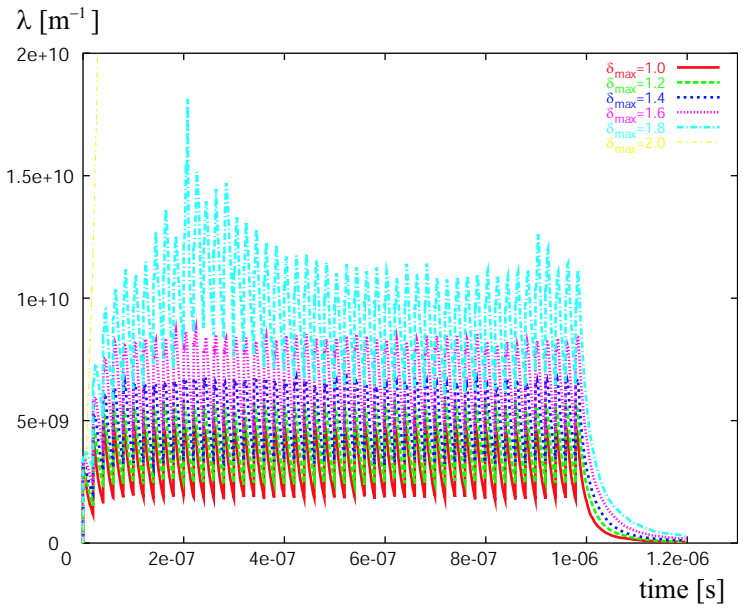

Figure 14: Electron line density in units of m^{-1} as a function of time in s in a 1st order harmonic expansion of the TESLA/ILC wiggler field in Cartesian coordinates, assuming $dN_{e^-}/dz = 0.2$ photoelectrons per e^+ and meter; the various curves refer to six different values of $\delta_{\max}$.

using a recipe proposed by Korostelev. Here, first the radial magnetic field on a cylinder surface is computed by the MERMAID magnet-design code for a prototype of, e.g., a CLIC hybrid wiggler [9]. One then applies an azimuthal Fourier transform to this field [9],

$$B_r(r = R, \phi, z) = \sum_{m=0}^{\infty} B_m(r, \phi) \sin(m\phi) \; . \tag{3}$$

which is followed by another Fourier transform, this time in the z coordinate,

$$\tilde{B}_{m,p} = \frac{1}{\lambda_p} \int_0^{\lambda_w} dz \, e^{-i2\pi pz} \lambda_w B_m(R, z) \; . \tag{4}$$

From this, we can compute the coefficients

$$b_{m,p} = \frac{\lambda_w}{2\pi p} \frac{\tilde{B}_{m,p}}{I'_m(2\pi pR/\lambda_w)} \; , \tag{5}$$

which enter into the scalar magnetic potential

$$\Psi = \sum_{m=0}^{\infty} \sum_{p=-\infty}^{\infty} e^{2\pi ipz/\lambda_w} I_m \left(\frac{2\pi p}{\lambda_w} r \right) b_{m,p} \sin(m\phi) \; . \tag{6}$$

The magnetic field at any point inside the vacuum chamber is finally obtained as

$$\vec{B} = \vec{\nabla} \cdot \Psi \; . \tag{7}$$

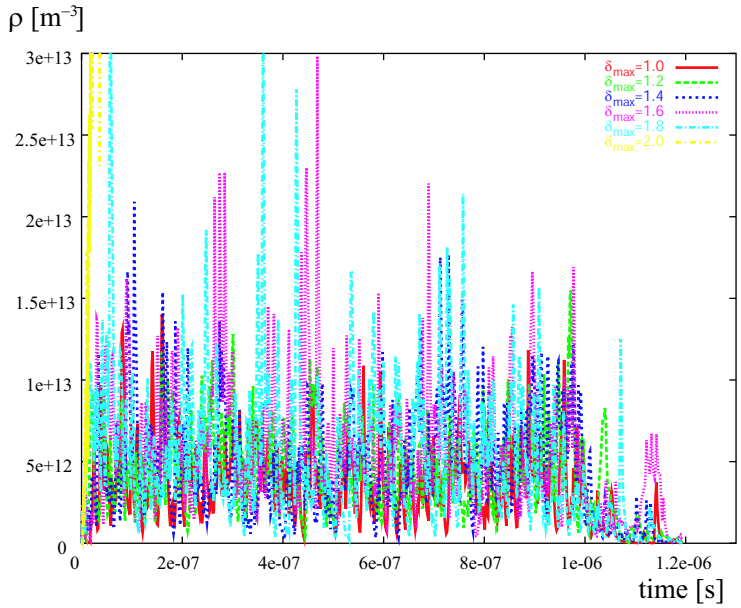

Figure 15: Central electron cloud volume density in units of m^{-3} as a function of time in s in a 1st order harmonic expansion of the TESLA/ILC wiggler field in Cartesian coordinates, assuming $dN_{e^-}/dz = 0.2$ photoelectrons per e^+ and meter; the various curves refer to six different values of $\delta_{\max}$.

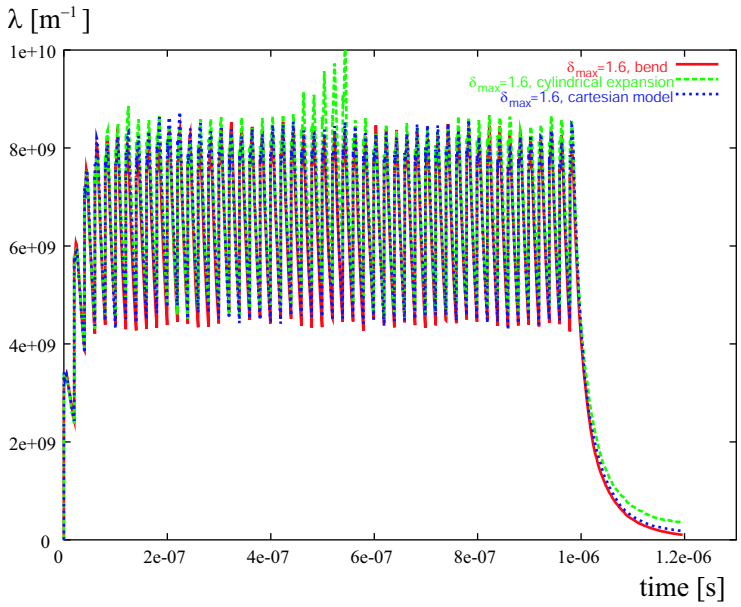

Figure 16: Electron line density in units of m^{-1} as a function of time in s for $\delta_{\max} = 1.6$, comparing the three different models of the TESLA/ILC wiggler field (constant bend, first term in a cylindrical expansion, first term in a harmonic expansion), assuming $dN_{e^-}/dz = 0.2$ photoelectrons per e^+ and meter.

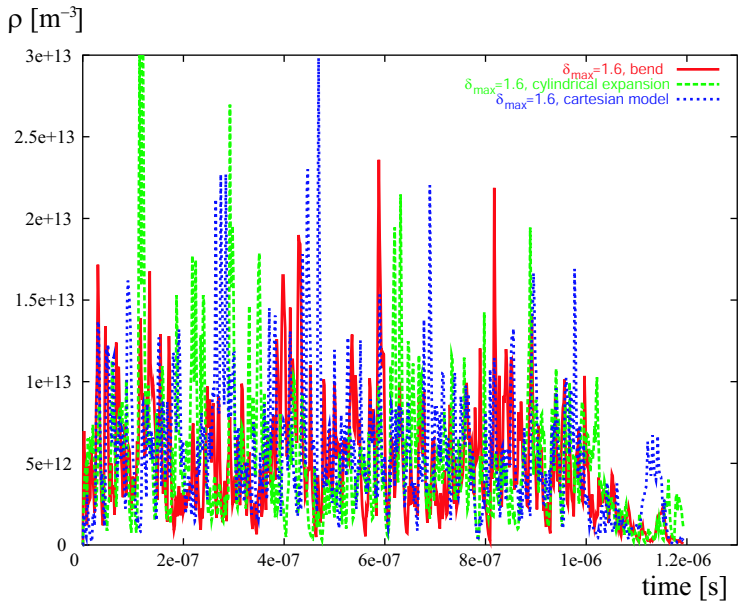

Figure 17: Central electron cloud volume density in units of m^{-3} as a function of time in s for $\delta_{\max} = 1.6$, comparing the three different models of the TESLA/ILC wiggler field (constant bend, first term in a cylindrical expansion, first term in a harmonic expansion), assuming $dN_{e^-}/dz = 0.2$ photoelectrons per e^+ and meter.

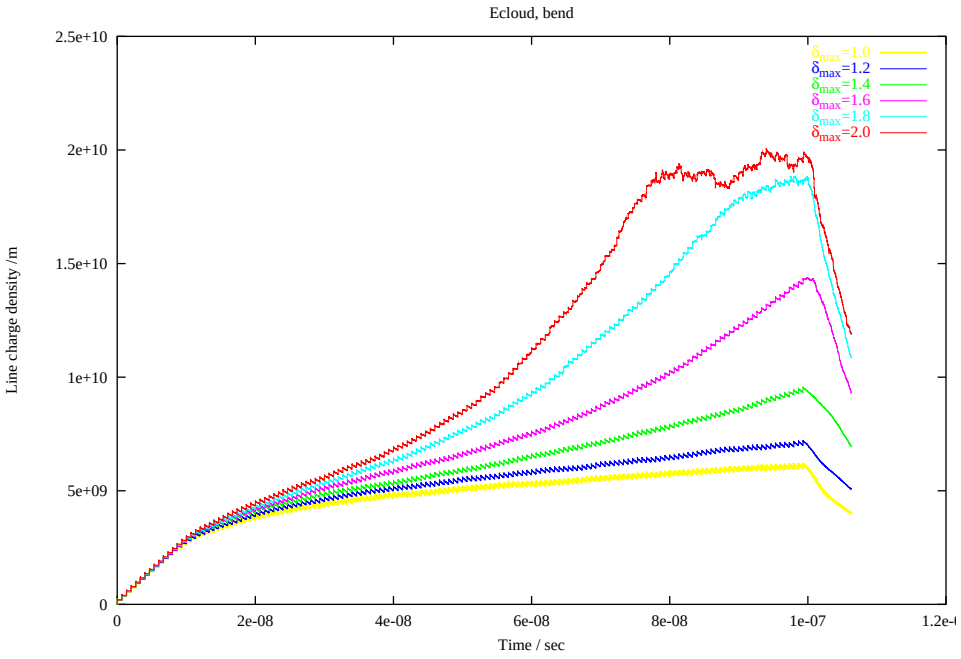

Figure 18: Electron line density in units of m^{-1} as a function of time in s for a bend with a field strength equivalent to the peak magnetic field strength of the CLIC wiggler magnet (1.76 T), assuming $dN_{e^-}/dz = 0.0576$ photoelectrons per e^+ and meter; the various curves refer to six different values of $\delta_{\max}$. Shown is the passage of 154 bunches followed by a gap.

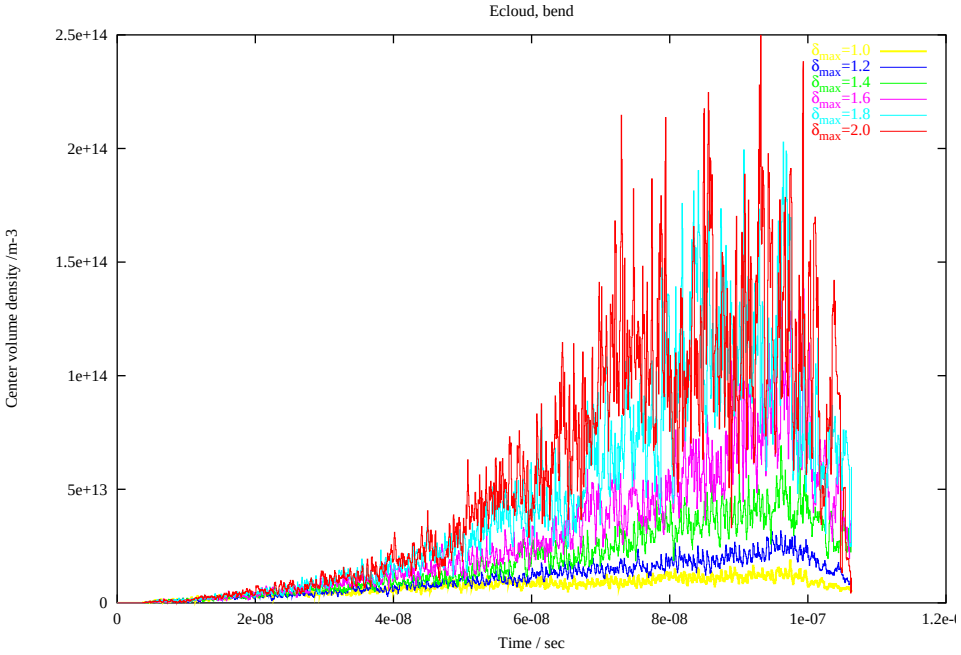

Figure 19: Central electron cloud volume density in units of m^{-3} as a function of time in s for a bend with a field strength equivalent to the peak magnetic field strength of the CLIC wiggler magnet (1.76 T), assuming $dN_{e^-}/dz = 0.0576$ photoelectrons per e^+ and meter; the various curves refer to six different values of $\delta_{\max}$. Shown is the passage of 154 bunches followed by a gap.

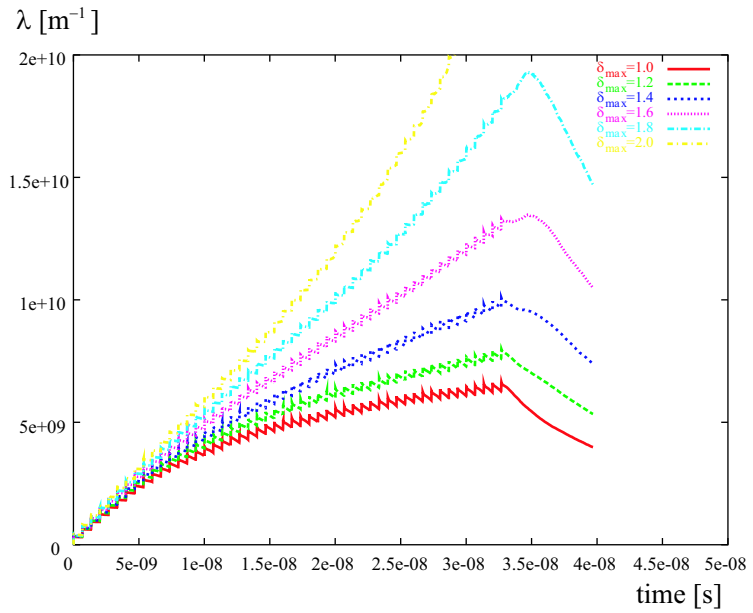

Figure 20: Electron line density in units of m^{-1} in units of m^{-3} as a function of time in s for a 1st order harmonic expansion of the CLIC wiggler field in Cartesian coordinates, assuming $dN_{e^-}/dz = 0.11$ photoelectrons per e^+ and meter; the various curves refer to six different values of $\delta_{\max}$. Shown is the passage of 50 bunches followed by a gap.

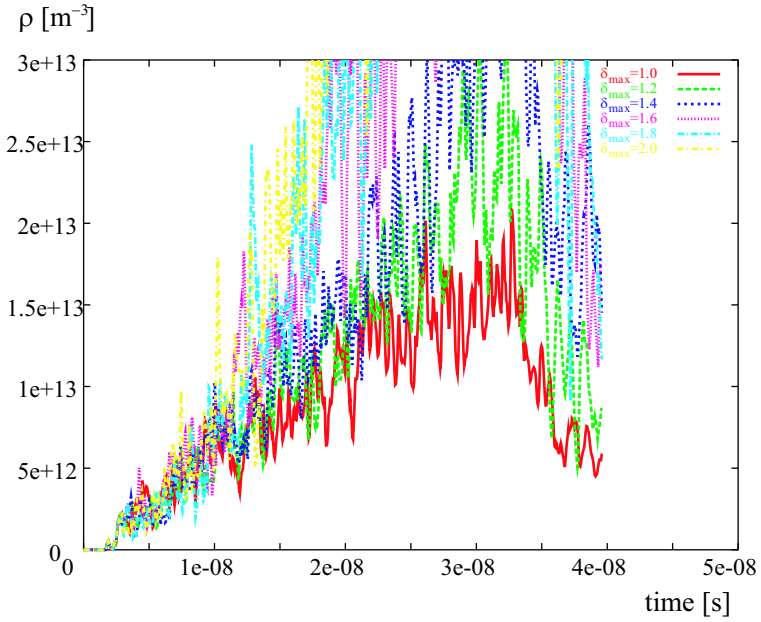

Figure 21: Central electron cloud volume density in units of m^{-3} as a function of time in s for a 1st order harmonic expansion of the CLIC wiggler field in Cartesian coordinates, assuming $dN_{e^-}/dz = 0.11$ photoelectrons per e^+ and meter; the various curves refer to six different values of $\delta_{\max}$. Shown is the passage of 50 bunches followed by a gap.

5 Electron-Cloud Instabilities

The electron cloud can induce multi-bunch [10] and single-bunch instabilities [11, 12]. The single-bunch instabilities have limited the performance of the two B factories and are considered as more severe, since the multi-bunch instabilities may, in principle, be suppressed with a bunch-by-bunch feedback system.
We study the single-bunch instability for the TESLA/ILC and CLIC damping rings using the code HEADTAIL [13]. Simulation parameters are listed in Table 2.
For TESLA/ILC we optimistically assume that the electron cloud is present only in the wiggler, while for CLIC the photo-electrons are pessimistically taken to be distributed all around the ring. Based on the photon-flux simulations in Section 3 we would rather expect the opposite situation, namely that in CLIC the antechambers efficiently intercept all photons in the arcs, whereas in TESLA/ILC non-intercepted photo-electrons remain in the arcs and even in the long straights. In the TESLA/ILC simulations, synchrotron motion is applied only once per turn, taking into account that both wigglers are installed in the same long straight section without any significant momentum compaction in between. For CLIC, the synchrotron motion takes place twice per turn, since the two long wiggler sections in CLIC are interleaved with the two arcs.

Table 2: Parameters for TESLA/ILC and CLIC instability simulations with HEADTAIL.

variable	TESLA/ILC	CLIC
electron density	$1 - 6 \times 10^{12}$ m^{-3} (wiggler)	$0.01 - 4 \times 10^{12}$ m^{-3} (average)
bunch population	2×10^{10}	4.2×10^{9}
hor. and vert. beta function	10.5 m	4, 7 m
rms bunch length	6 mm	1.3 mm
horizontal rms beam size	93 micron	23 micron
vertical rms beam size	5 micron	3.5 micron
rms momentum spread	1.3×10^{-3}	1.3×10^{-3}
synchrotron tune	0.07	0.005
momentum compaction	0.12×10^{-3}	0.731×10^{-4}
circumference (wiggler length)	17 km (540 m)	357 m
relativistic Lorentz factor	9785	4744
number of e^--beam interactions / turn	5–30	5–30
hor. & vert. betatron tune	72.28, 44.18	72.85, 34.82

Figure 22 shows the simulated emittance growth for various cloud densities in the TESLA/ILC wiggler. A weak-instability threshold is visible at a wiggler electron density of $\rho_{wiggler} \approx 2 \times 10^{12}$ m^{-3}, below the typical density value of 5×10^{12} m^{-3} found in electron build-up simulations (see Section 4). The rise times are small. Comparing the emittance growth rate of $1/\tau_\epsilon \approx 1.3$ s^{-1} at $\rho_{wiggler} \approx 4 \times 10^{12}$ m^{-3} with the transverse

radiation damping time of $2\tau_s \approx 56$ ms, we estimate an equilibrium emittance blow up of $\tau_s/\tau_\epsilon \approx 4$ % for this density. We recall that these numbers, for ILC/TESLA, assume the absence of an electron cloud in all non-wiggler sections of the ring.

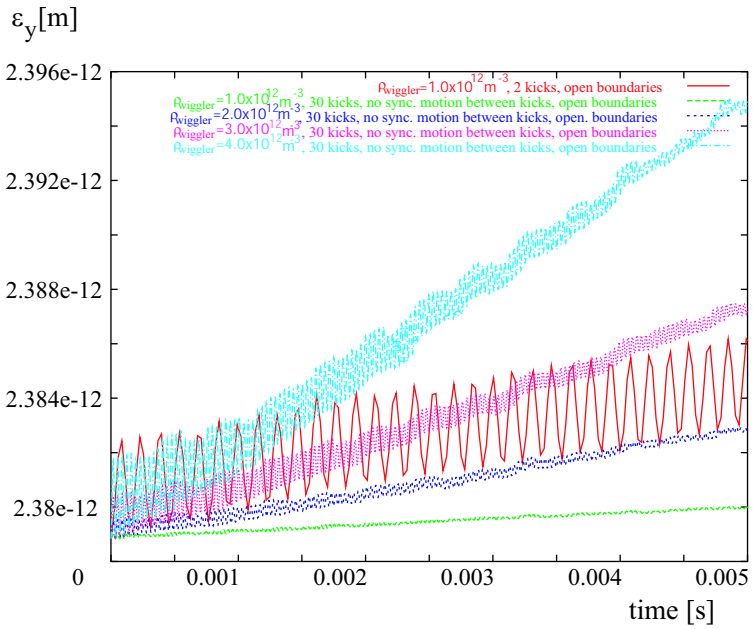

Figure 22: Simulated vertical geometric emittance in TESLA/ILC as a function of time for various unperturbed electron-cloud densities in the wiggler without synchrotron motion between the 30 IPs applied on each turn (exccept for the oscillating curve which refers to 2 kicks); other parameters are listed in Table 2; open boundaries are used.

Simulation results for CLIC are presented in Fig. 23. A weak instability occurs above $\rho_{ring} \approx 1 \times 10^{12}$ m^{-3}, which is a value 20 times lower than the density after 30 ns simulated for the Cartesian field model (Fig. 21).

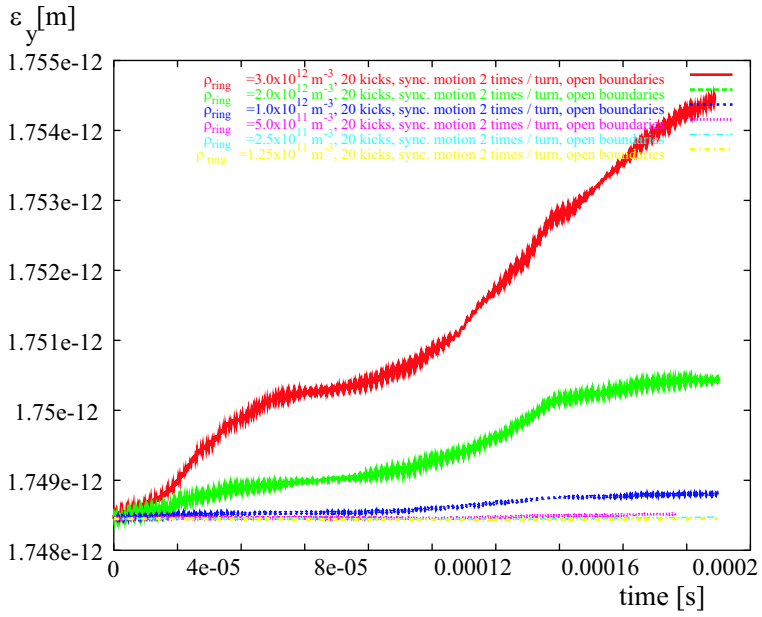

Figure 23: Vertical geometric emittance in CLIC as a function of time for different unperturbed electron-cloud densities (average around the ring) for 20 electron-beam interaction points per turn; other parameters are listed in Table 2.

6 DAFNE

The DAFNE observations are summarized as follows. In 2004/05, the positron current with 100–110 bunches has been limited to about 1.4 A in collision by a strong instability, with about 10 μs rise time. It is not yet completely clear whether this instability has a coupled- or single-bunch nature. In the old fill pattern, used in 2002, with about 50 bunches, separated by empty buckets, the maximum current is now restricted to 0.4–0.5 A by the instability, while in previous years, until 2002, 1.2 A of current could be reached without any noticable sign of instability. Also, in the positron ring, presently a large positive horizontal tune shift with intensity of about 0.01 at 600 mA beam current is observed, to be compared with a tune shift of 0.002 for the electron ring [14]. The tune shift of 0.01 is comparable to the electron-cloud induced tune shifts seen at the CERN SPS and the KEK B factory. In a simple model of a uniform cloud the average electron density is related to the coherent tune shift ΔQ via [15]

$$\rho_e \approx \frac{2\gamma\Delta Q}{r_e C < \beta >} , \tag{8}$$

which for DAFNE, with $< \beta > \approx$ 3.5 m (in the wiggler), would yield the estimate $\rho_e \approx 2 \times 10^{13}$ m^{-3}, which is more than 10 times higher than in other present machines. Given the fairly small fraction of the ring occupied by the wigglers (about 8%), the local electron density inside the wiggler would need to be of order 2×10^{14} m^{-3}, if the cloud is present only in the wigglers.

In an attempt to find a remedy, following the example of KEKB and PEP-II solenoids were wound in the field-free regions of DAFNE, without any effect on the instability. The main hardware change for the 2004-run was a modification of the wiggler poles smoothing the wiggler field. The appearance of the instability after this modification gives rise to the suspicion that electrons are trapped by the wiggler field. The instability is sensitive to the orbit in the wiggler: the threshold varies by factors of two for orbit changes of a few mm. This may be consistent with the hypothesis that a local electron cloud inside the wiggler drives the instability. The instability threshold seems to depend on the bunch current, not on the total current, as discussed in [16]. It strongly increases along the train, which could be explained by the build up of electrons along the train and/or by the beam break-up nature of an electron-driven coupled-bunch instability. The instability rise time is faster than the synchrotron period, the instability is sensitive to the injection conditions, and the instability threshold scales with the transverse emittance. As pointed out in [17], DAFNE is the only storage ring operating in the 'short-bunch' regime of the single-bunch instability, for which the growth rate scales as $1/\sqrt{\epsilon_x \epsilon_y} \sim 1/\epsilon_x$. This dependence suggests one possible explanation for the instability threshold reduction, since in the 2004-05 run the horizontal emittance was decreased by a factor of two to alleviate the parasitic crossing effects on the luminosity.

Figure 24 shows a grow-damp measurement for the horizontal positron-beam instability, recorded by A. Drago [14]. In this example, 90 consecutive bunches were followed by a gap of 30 missing bunches. The total beam current was 500 mA. The figure shows the onset of instability and subsequent feedback damping for bunches 75, 80, 85 and 90, at

the end of the train, illustrating that the growth rate strongly increases with the bunch number.

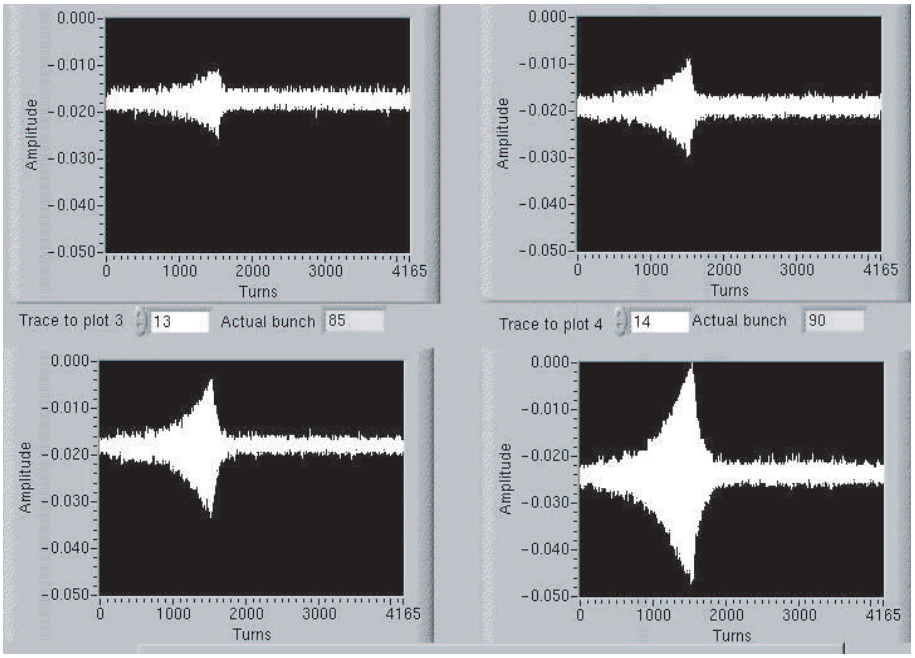

Figure 24: Horizontal growth-damp measurements for bunches 75, 80, 85, and 90, of the DAFNE positron beam for a total beam current of 500 mA. Shown is the turn-by-turn position offset. The horizontal feedback is switched off during 500 μs (Courtesy A. Drago) [14].

In order to simulate the electron build up with the nonlinear field components of the DAFNE wiggler before and after the wiggler modifications, we have implemented yet a different wiggler-field model in the ECLOUD code, where the vertical magnetic field inside the wiggler as a function of the three Cartesian coordinates is obtained from a bi-cubic spline fit of the measured two-dimensional field map data $B_y(x, y = 0, z)$. The three field components are approximated by

$$\begin{aligned} B_x(x,y,z) &\approx \frac{\partial B_y(x,y=0,z)}{\partial x}\, y \\ B_z(x,y,z) &\approx \frac{\partial B_y(x,y=0,z)}{\partial z}\, y \\ B_y(x,y,z) &\approx B_y(x,y=0,z) \\ &\quad -\frac{y^2}{2}\left(\frac{\partial^2 B_y(x,y=0,z)}{\partial x^2}\right. \\ &\quad \left. +\frac{\partial^2 B_y(x,y=0,z)}{\partial z^2}\right) , \end{aligned} \tag{9}$$

where the last equation is a modified version of [18], in order to be consistent with

$$\begin{aligned} \vec{\nabla} \times \vec{B} &= 0\,, \\ \vec{\nabla} \cdot \vec{B} &= 0\,. \end{aligned} \tag{10}$$

Figure 25 displays the vertical magnetic field measured after the pole modification as a function of longitudinal position for three different horizontal offsets. The peak central wiggler peak field is about 1.7 T and the period 65 cm. The vertical field reconstructed by the ECLOUD code using the bi-cubic spline fit is presented in Fig. 26. It appears to be an excellent approximation to the measured field in Fig. 25. The horizontal and longitudinal fields were not measured, but they can also be derived from the bi-cubic fit, using the relations (9). They are shown in Figs. 27 and 28.
A similar model was constructed for the wiggler field before the wiggler-pole modification, from a fit to earlier field measurements. The corresponding vertical, horizontal and longitudinal fields are displayed in Figs. 29, 30, and 31. We do not find any qualitative difference in the appearance of the various field components before and after the wiggler modifications.

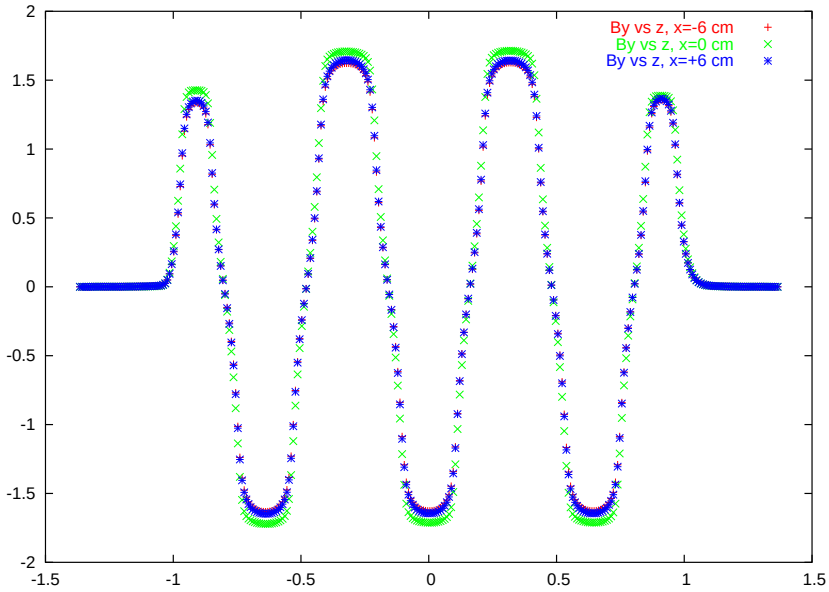

Figure 25: Measured vertical magnetic field in the DAFNE wiggler after pole modification as a function of longitudinal position. The top green curve refers to the horizontal center of the magnet, the red and blue curves show values measured with a horizontal offset of -6 cm and $+6$ cm, respectively.

Using this refined model of the DAFNE wiggler field and the parameters of Table 1, the electron build up in DAFNE was simulated. We considered a maximum secondary emission yield $\delta_{\max} \approx 1.9$ and a primary electron energy corresponding to the maximum of $\epsilon_{\max} \approx 300$ eV, as were found for technical aluminium surfaces after electron conditioning [19]. In the DAFNE simulations, the elastic reflection probability in the limit of zero

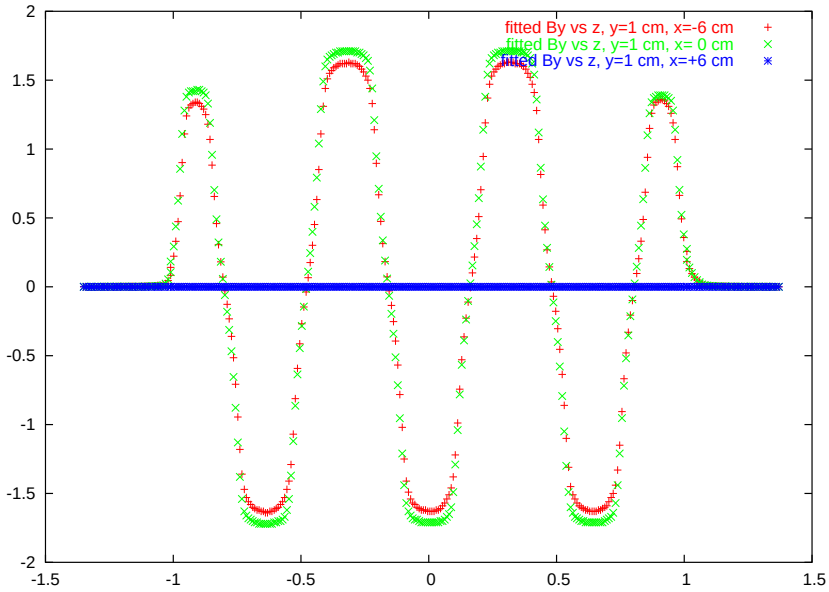

Figure 26: Vertical magnetic field in the DAFNE wiggler after pole modification, reconstructed from a bi-cubic spline fit in the ECLOUD code, as a function of longitudinal position. The top green curve refers to the horizontal center of the magnet, the red and blue curves show values measured with a horizontal offset of -6 cm and $+6$ cm, respectively, and a vertical offset of 1 cm.

incident energy is taken to be 50%, based on the SPS benchmarking [20]. Unlike for the TESLA and CLIC damping ring, in the DAFNE simulations 20% of the photo-electrons are taken to be reflected photons with a $\cos^2\phi$ distribution (where ϕ here denotes the angle to the photon emission point with respect to the horizontal plane, viewed from the primary light impact point at the chamber wall [21]), while the other photons are emitted in a narrow angular range from the horizontally outward side of the chamber. We note that even higher photon reflectivities, of 50–60%, were measured by R. Cimino for a DAFNE aluminium vacuum chamber [2].

Simulation results over one revolution period for both the present and the 2002 beam parameters, in both cases assuming the same 2004/05 wiggler field, are displayed in Fig. 32. For 2002 we take 50 bunches with a bunch population of $N_b = 4.28 \times 10^{10}$, spaced by 1.6 m, followed by a gap of 10 missing bunches. For 2005, 100 bunches spaced by 0.8 m, and with a bunch population of 2.1×10^{10} are followed by a gap of 20 missing bunches. The beam sizes also differ (see Table 3 below). Figure 32 demonstrates that for the same model of the new 2004/05 wiggler field, the old 2002 beam parameters lead to a nonlinear increase of the electron density due to beam-induced multipacting to a line density of 5×10^{10} m^{-3} (where the bunch train ends), while for the new the electron density grows more gradually and reaches a final line density of 10^{10} m^{-1}. The final line density for the 2004/05 beam parameters corresponds to an average volume density inside the wiggler of 4×10^{12} m^{-3}, while for the 2002 beam parameters it is 2×10^{13} m^{-3}. The latter value is consistent with the density estimated from the measured tune shift, if

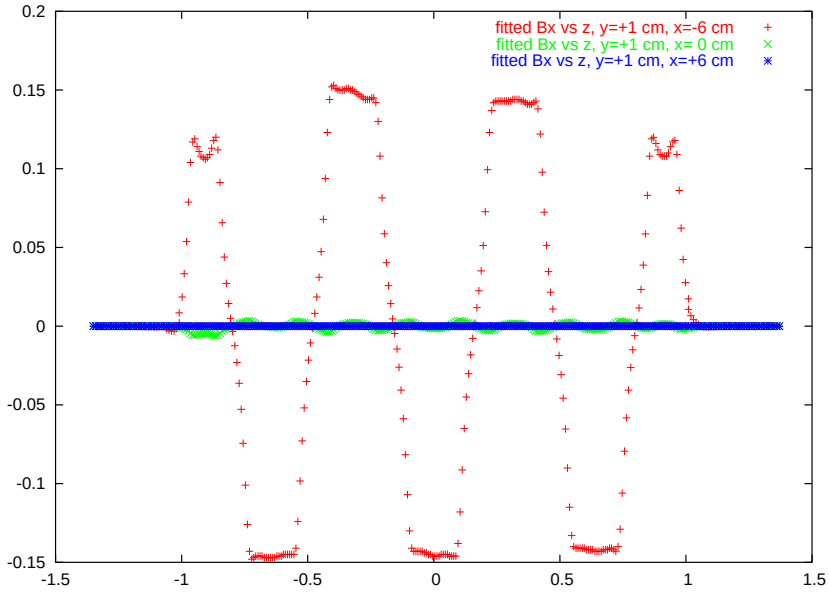

Figure 27: Horizontal magnetic field in the DAFNE wiggler after pole modification, reconstructed from a bi-cubic spline fit in the ECLOUD code, as a function of longitudinal position. The top green curve refers to the horizontal center of the magnet, the red and blue curves show values measured with a horizontal offset of -6 cm and $+6$ cm, respectively, and a vertical offset of 1 cm.

the cloud is present all around the ring (if the cloud is concentrated only in the wiggler, a 10 times larger local density would be required to explain the observed tune shift). Figure 33 illustrates, for the identical 2002 beam parameters, that the electron build up is two times larger at the end of the bunch train for the new wiggler field as compared with the old one. Figure 34 presents the horizontal distribution of electrons at the end of a turn for the 2004/05 DAFNE wiggler and 2002 beam parameters, i.e., the case with strongest multipacting. The figure reveals the presence of two vertical stripes of multipacting electrons on either side of the beam, at a horizontal distance of about 4 mm from the center.

The instability in DAFNE could be either of the coupled-bunch or single-bunch type. The multibunch wake field W [m^{-2}] can be computed by the ECLOUD code. To this end, one bunch is transversely displaced by a prescribed offset and the resulting force (central electric field) for all subsequent bunches is recorded. The multibunch wake fields, W_x and W_y, are obtained from the fields E_x or E_y via

$$\begin{aligned} W_x &= \frac{1}{r_e}\left(\frac{eE_x}{m_e}\right)\frac{L_{w,tot}}{N_b \Delta x}\frac{1}{c^2} \\ &\approx \begin{cases} 1\times 10^{-9}\ \mathrm{s^2 m^{-3}}\left(\frac{eE_x}{m_e}\right) & (2004) \\ 5\times 10^{-10}\ \mathrm{s^2 m^{-3}}\left(\frac{eE_x}{m_e}\right) & (2002) \end{cases}, \end{aligned} \tag{11}$$

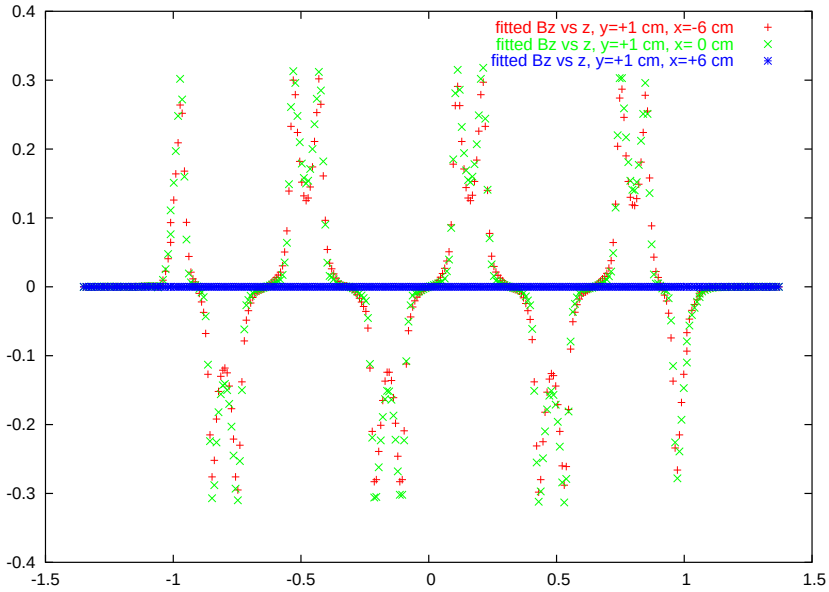

Figure 28: Longitudinal magnetic field in the DAFNE wiggler after pole modification, reconstructed from a bi-cubic spline fit in the ECLOUD code, as a function of longitudinal position. The top green curve refers to the horizontal center of the magnet, the red and blue curves show values measured with a horizontal offset of -6 cm and $+6$ cm, respectively, and a vertical offset of 1 cm.

and

$$W_y = \frac{1}{r_e}\left(\frac{eE_y}{m_e}\right)\frac{L_{w,tot}}{N_b \Delta y}\frac{1}{c^2} \approx \begin{cases} 3\times 10^{-8}\ \mathrm{s^2 m^{-3}}\left(\frac{eE_y}{m_e}\right) & (2004) \\ 2\times 10^{-8}\ \mathrm{s^2 m^{-3}}\left(\frac{eE_y}{m_e}\right) & (2002) \end{cases}, \tag{12}$$

where the numerical values refer to the 2004 and 2002 conditions, an offset $\Delta x = 1.3$ or 1.4 mm (equal to 1 σ_x), or $\Delta y = 0.04$ or 0.05 mm (equal to 1 σ_y), a bunch population $N_b = 2.1\times 10^{10}$ or 4.28×10^{10}, respectively, and to a total wiggler length $L_{w,tot}$ of about 8 m. From the multibunch wake field, the coupled-bunch instability rise time can be estimated as

$$\tau_{CB} \approx \frac{2\gamma C \omega_\beta}{N_b r_e c^2 W(L_{\mathrm{sep}})} \approx \begin{cases} 3.7\ \frac{\mathrm{s}}{\mathrm{m}^2}\ \frac{1}{W(L_{\mathrm{sep}})} & (2004) \\ 1.8\ \frac{\mathrm{s}}{\mathrm{m}^2}\ \frac{1}{W(L_{\mathrm{sep}})} & (2002) \end{cases}. \tag{13}$$

Figures 35 and 36 display the horizontal coupled-bunch wake fields computed for the 2004 and 2002 wiggler and beam parameters, respectively. The wake field was obtained by subtracting the electric field computed without bunch offset from the field calculated when one bunch was displaced. The multi-bunch wake field simulated for the new beam parameters with the new wiggler field is two orders of magnitude smaller than the one for the 2002 conditions. However, assuming the 2002 beam parameters for the 2004/05 wiggler field (see Fig. 37), the simulated multi-bunch wake field increases by about a factor of two, as is illustrated in Fig. 38.

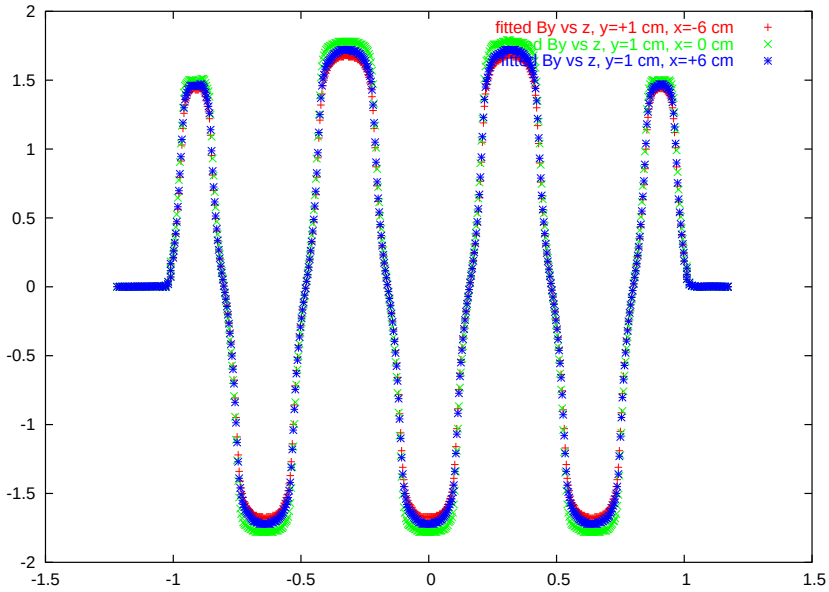

Figure 29: Vertical magnetic field in the DAFNE wiggler prior to pole modification, reconstructed from a bi-cubic spline fit in the ECLOUD code, as a function of longitudinal position. The top green curve refers to the horizontal center of the magnet, the red and blue curves show values measured with a horizontal offset of -6 cm and $+6$ cm, respectively, and a vertical offset of 1 cm.

The multi-bunch rise time estimated from (13) for the 2002 beam parameters with either the new or old wiggler parameters, differing by a factor of two, varies between less than 10 μs and a few 100 ms, depending on wether we consider for $W(L_{\rm sep})$ the maximum amplitude of the wake or the wake experienced by the bunch following the displaced bunch. In any case, (13) only provides an extremely rough estimate, as it is based on the assumption that the electron-cloud wake only couples successive bunches, which is clearly violated by the simulated wake field.

We finally explore the possibility of a single-bunch instability. Pertinent simulations were performed with the code HEADTAIL [13] for the two sets of parameters listed in Table 3, again roughly approximating the conditions before and after the wiggler modifications. In these simulations, the wiggler field was modeled as a strong dipole. Simulation results are displayed in Figs. 39–42, for average electron densities over the ring varying between 5×10^{12} m^{-3} and 2×10^{13} m^{-3} (equivalent to densities in the wiggler of about $6.\times10^{13}$ m^{-3} to 2.5×10^{14} m^{-3}). Both in the horizontal plane (Figs. 41 and 42), and in the vertical plane (Figs. 39 and 40), the simulations show the threshold of a strong single-bunch instability at average electron densities around the ring between 10^{13} m^{-3} and 2×10^{13} m^{-3} (or at equivalent local electron densities in the wiggler only between 1.3×10^{14} m^{-3} and 2.5×10^{14} m^{-3}). The simulated threshold densities agree well with the average electron density estimated from the measured tune shift, and are comparable with the electron density simulated for the old beam parameters with the new field. The instability rise time above threshold is less than 100 μs in all cases.

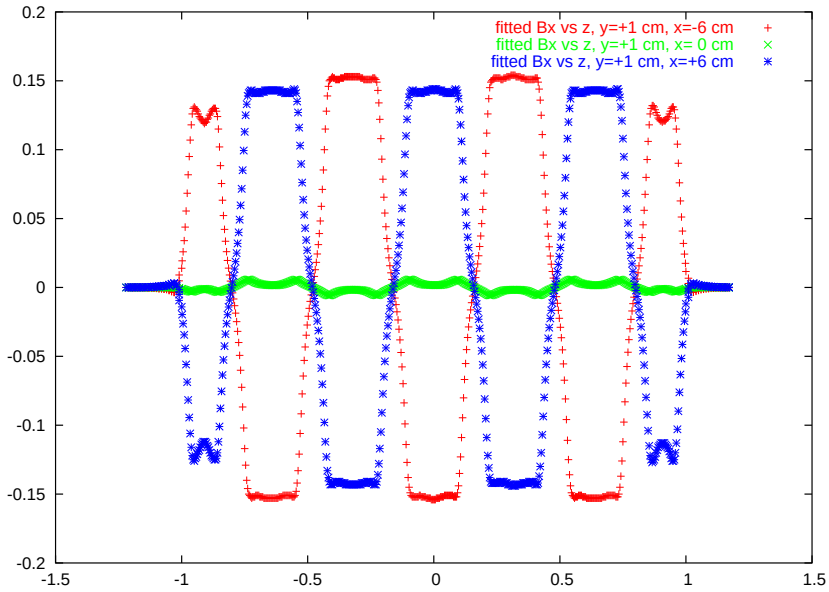

Figure 30: Horizontal magnetic field in the DAFNE wiggler prior to pole modification, reconstructed from a bi-cubic spline fit in the ECLOUD code, as a function of longitudinal position. The top green curve refers to the horizontal center of the magnet, the red and blue curves show values measured with a horizontal offset of -6 cm and $+6$ cm, respectively, and a vertical offset of 1 cm.

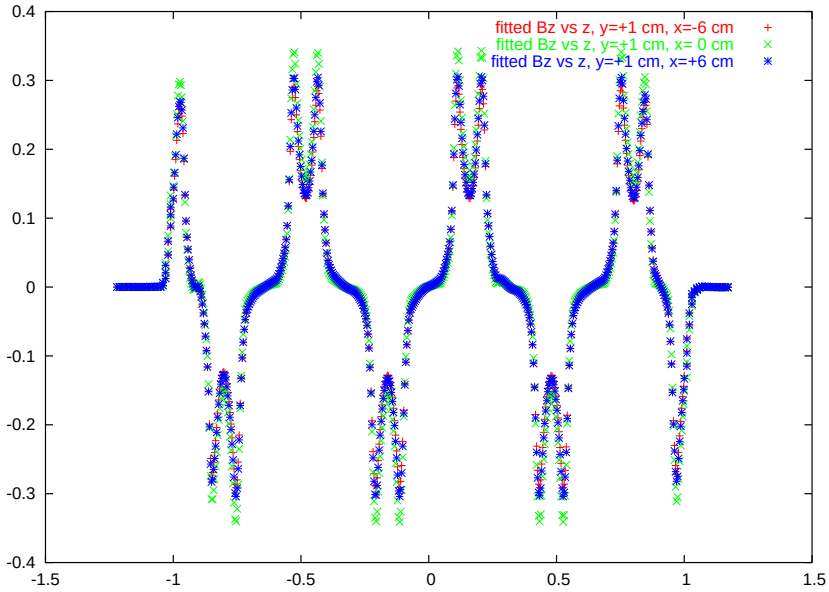

Figure 31: Longitudinal magnetic field in the DAFNE wiggler prior to pole modification, reconstructed from a bi-cubic spline fit in the ECLOUD code, as a function of longitudinal position. The top green curve refers to the horizontal center of the magnet, the red and blue curves show values measured with a horizontal offset of -6 cm and $+6$ cm, respectively, and a vertical offset of 1 cm.

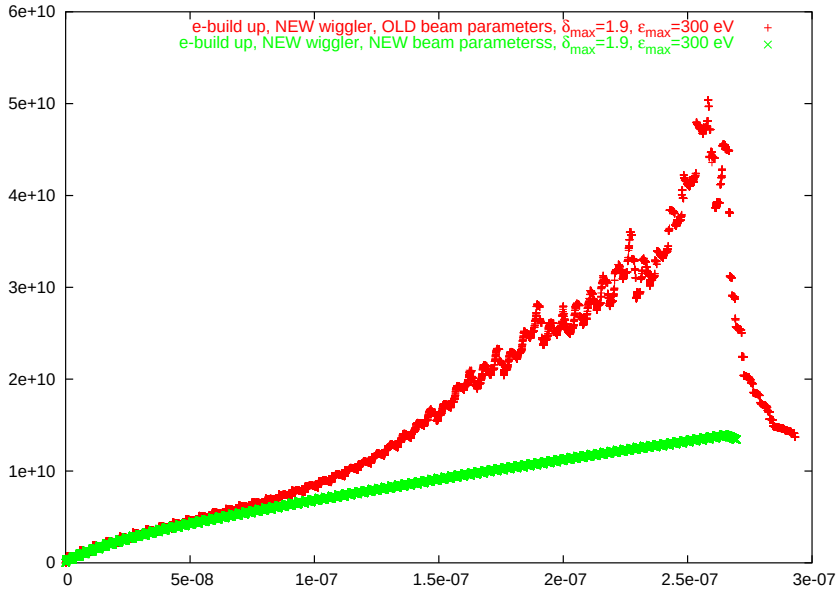

Figure 32: Simulated electron line density in units of m^{-1} as a function of time in s for the 2004 DAFNE wiggler with old and new beam parameters, assuming $dN_{e^-}/dz = 0.018$ photoelectrons per e^+ and meter, $\delta_{\max} = 1.9$ and $\epsilon_{\max} = 300$ eV.

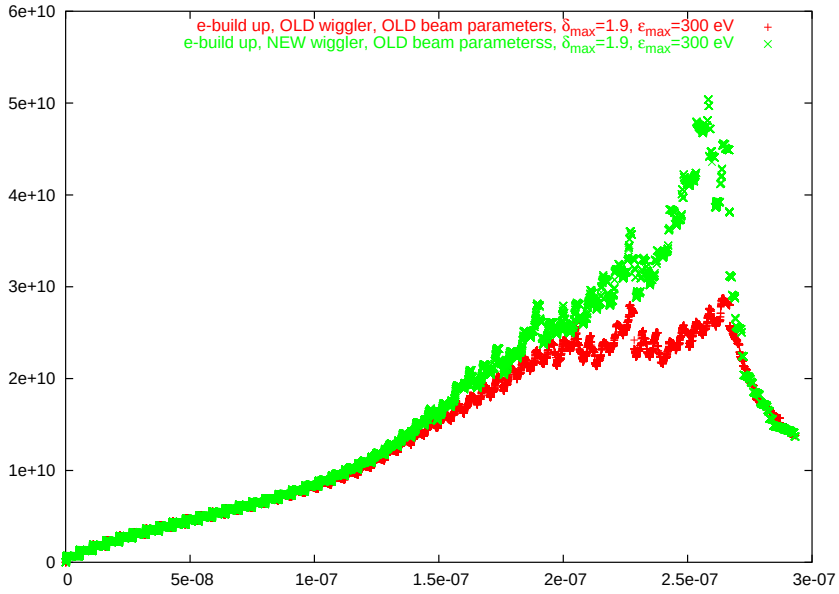

Figure 33: Simulated electron line density in units of m^{-1} as a function of time in s comparing the old and the new DAFNE wiggler, for the 2002 beam parameters; we assumed a maximum secondary emission yield $\delta_{\max} = 1.9$ at $\epsilon_{\max} = 300$ eV, and $dN_{e^-}/dz = 0.018$ photoelectrons per e^+ and meter.

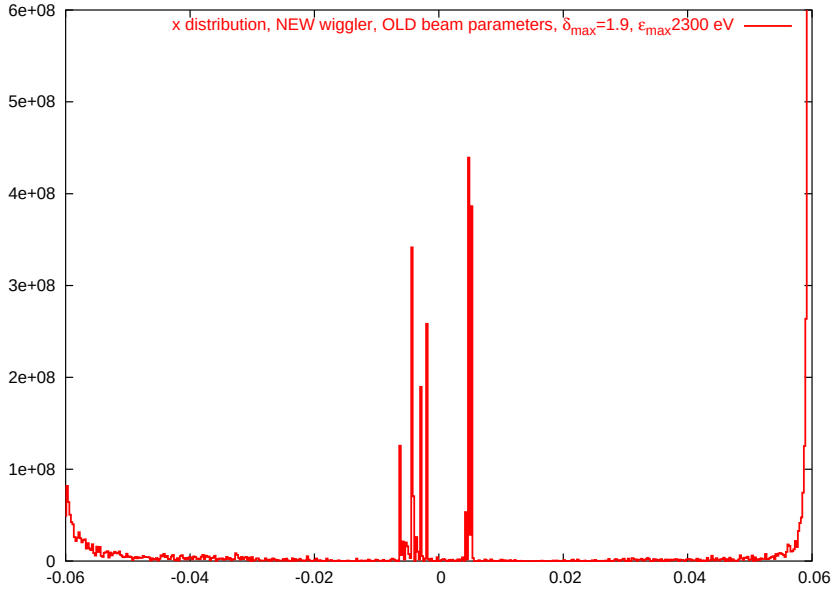

Figure 34: Horizontal electron distributions at the end of the simulation for the 2004/05 DAFNE wiggler with the 2002 beam parameters; we assumed a maximum secondary emission yield $\delta_{\max} = 1.9$ at $\epsilon_{\max} = 300$ eV, and $dN_{e^-}/dz = 0.018$ photoelectrons per e^+ and meter.

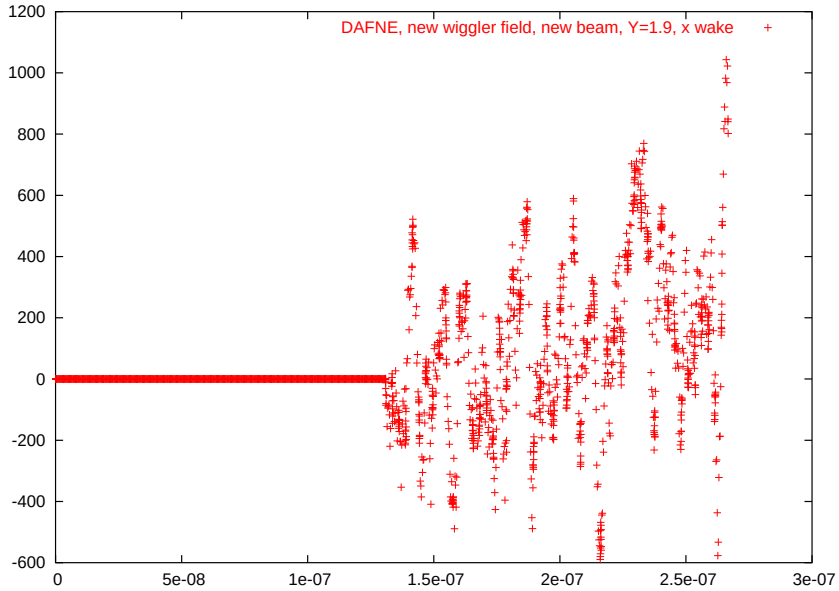

Figure 35: Multibunch wake field computed for the 2004 wiggler field and 2004 beam parameters. The 50th bunch of the train is displaced horizontally; the resulting wake field W for consecutive bunches is shown.

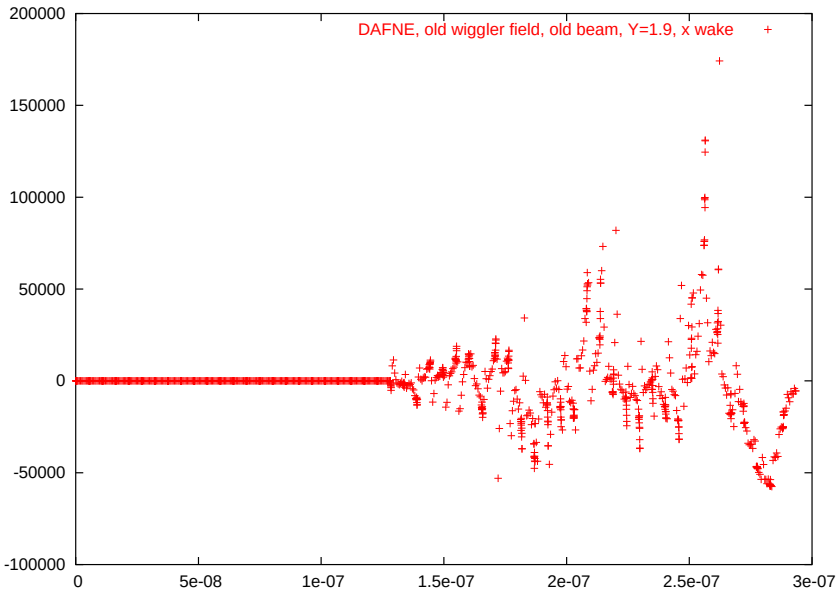

Figure 36: Multibunch wake field computed for the 2002 wiggler field and beam parameters. The 25th bunch of the train is displaced horizontally; the resulting wake field W for consecutive bunches is shown.

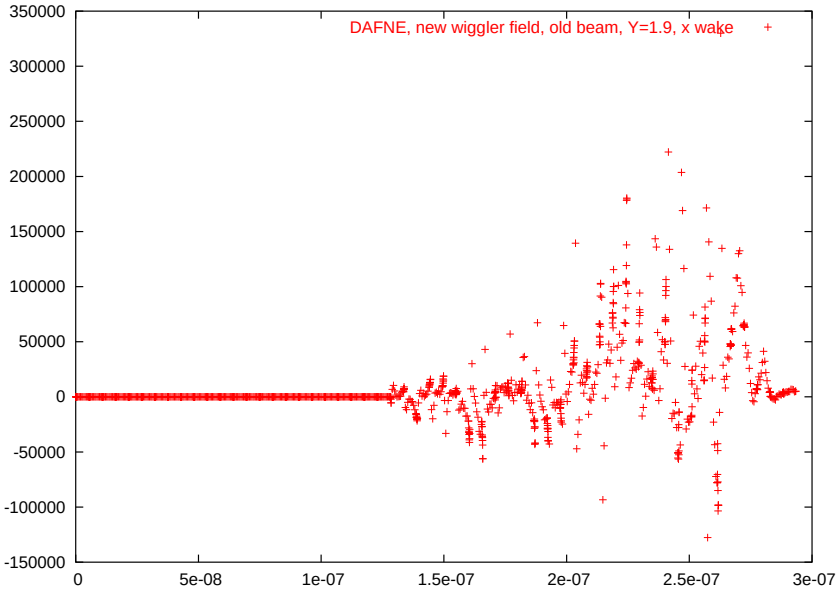

Figure 37: Multibunch wake field computed for the 2004 wiggler field and 2002 beam parameters. The 25th bunch of the train is displaced horizontally; the resulting wake field W for consecutive bunches is shown.

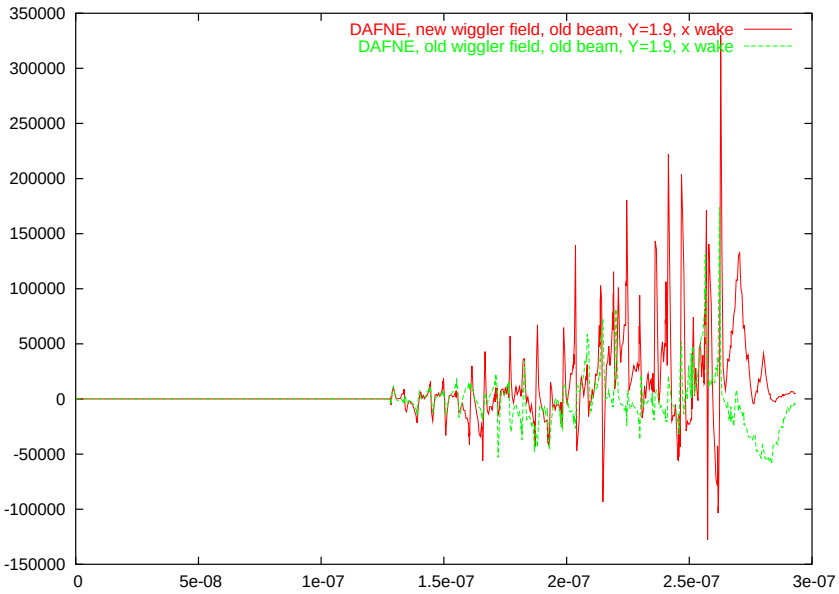

Figure 38: Multibunch wake field computed for the 2004 and 2002 wiggler fields (the two curves), and 2002 beam parameters. The 25th bunch of the train is displaced horizontally; the resulting wake field W for consecutive bunches is shown.

Table 3: Parameters for DAFNE single-bunch instability simulations with HEADTAIL.

variable	symbol	value	
		old wiggler (2002)	modified wiggler (2005)
bunch intensity	N_b	4.28×10^{10}	2.1×10^{10}
rms bunch length	σ_z	22 mm	17 mm
rms horizontal size	σ_x	1.4 mm	1.3 mm
rms vertical size	σ_x	0.05 mm	0.04 mm
horizontal beta function	β_x	2.4 m	3.4 m
vertical beta function	β_y	1.1 m	1.1 m
chromaticity	$Q'_{x,y}$	2	2
momentum compaction	α	0.023	0.023
synchrotron tune	Q_s	0.0083	0.0083
rf voltage	V_{rf}	80 kV	80 kV
rms momentum spread	$\Delta p/p$	4.4×10^{-4}	4×10^{-4}

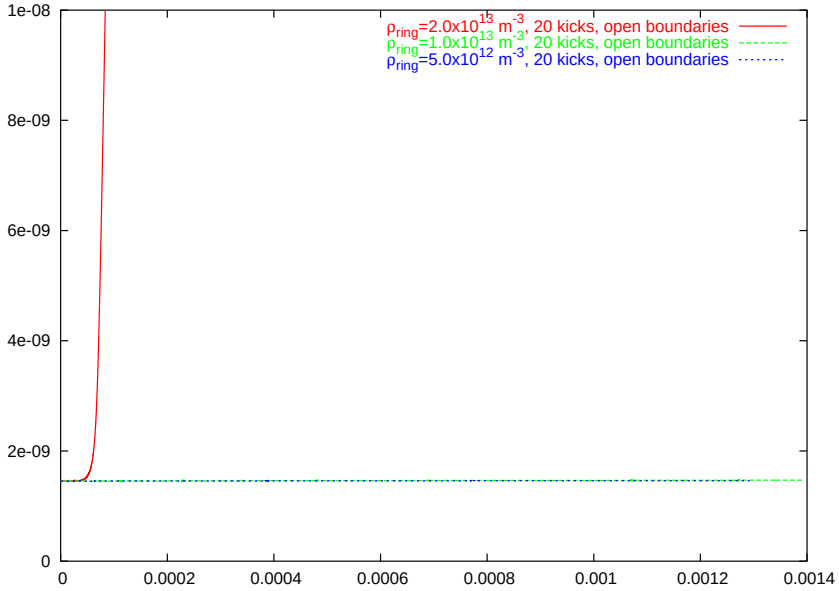

Figure 39: Vertical single-bunch geometric emittance in units of meter at DAFNE for the 2004/2005 conditions, as a function of time in seconds for various unperturbed average electron-cloud densities between 5×10^{12} m^{-3} and 2×10^{13} m^{-3}, simulated by HEADTAIL; parameters are listed in Table 3; open boundaries are used.

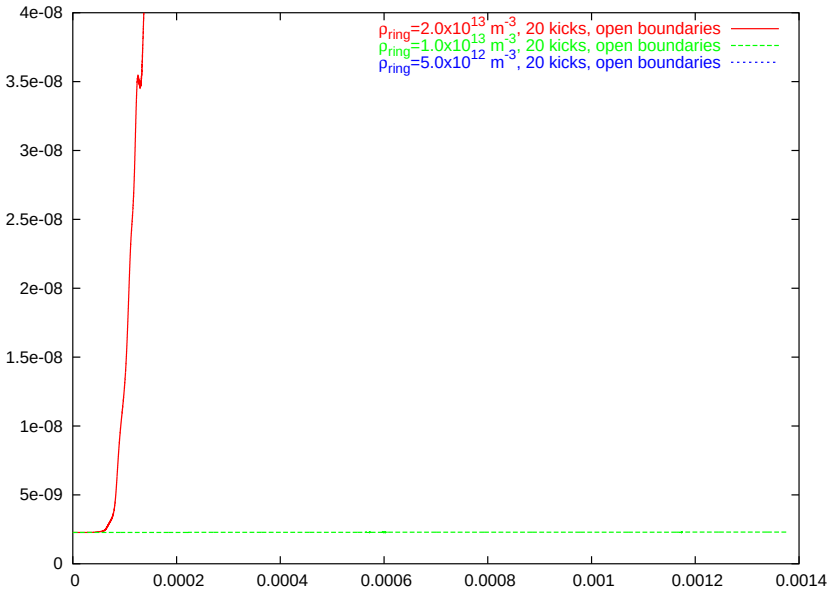

Figure 40: Vertical single-bunch geometric emittance in units of meter at DAFNE for the 2002 conditions, as a function of time in seconds for various unperturbed average electron-cloud densities between 5×10^{12} m^{-3} and 2×10^{13} m^{-3}, simulated by HEADTAIL; parameters are listed in Table 3; open boundaries are used.

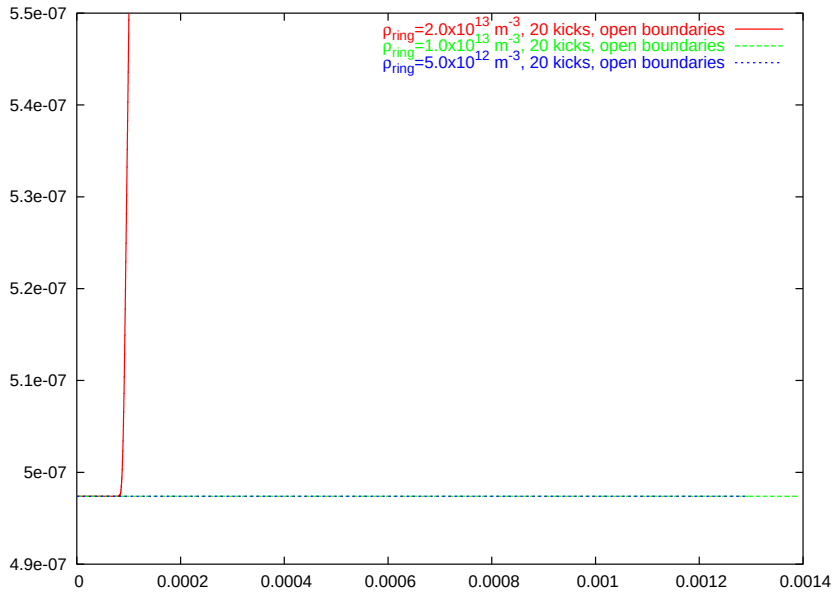

Figure 41: Horizontal single-bunch geometric emittance in units of meter at DAFNE for the 2004/2005 conditions, as a function of time in seconds for various unperturbed average electron-cloud densities between 5×10^{12} m^{-3} and 2×10^{13} m^{-3}, simulated by HEADTAIL; parameters are listed in Table 3; open boundaries are used.

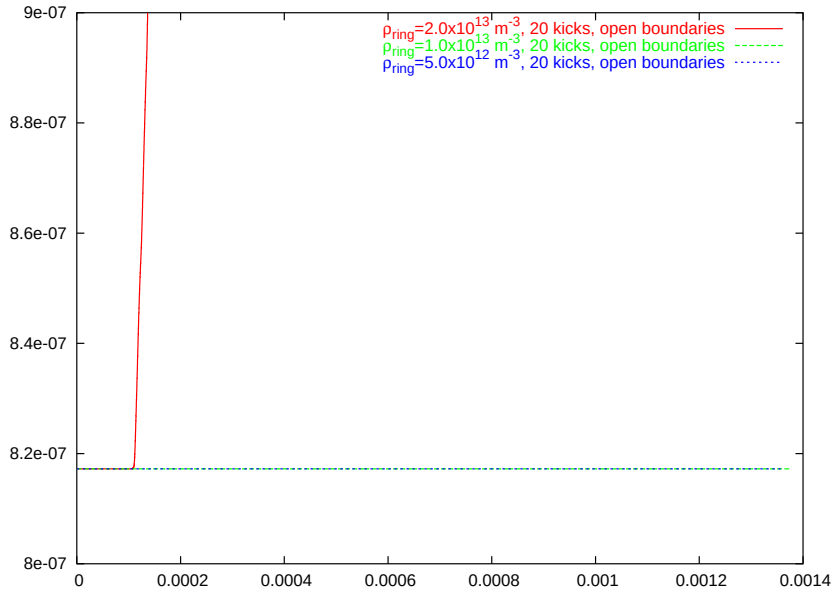

Figure 42: Horizontal single-bunch geometric emittance in units of meter at DAFNE for the 2002 conditions, as a function of time in seconds for various unperturbed average electron-cloud densities between 5×10^{12} m^{-3} and 2×10^{13} m^{-3}, simulated by HEADTAIL; parameters are listed in Table 3; open boundaries are used.

7 Conclusions

A significant fraction of the synchrotron-radiation photons emitted in linear-collider damping rings is not absorbed by the wiggler antechambers. Together with the high primary photon flux in the wigglers, a large rate of primary photoelectrons is, therefore, expected. In consequence, the simulated electron density in the wiggler is much higher than that for the arcs and the straight sections. For both CLIC and TESLA/ILC the density simulated with a more accurate field model is almost equal to that found for a uniform dipole field.
The electron cloud in the wiggler likely causes single- and multi-bunch electron-cloud instabilities. In particular, an electron cloud could be, fully or partly, responsible for the present current limitation in the DAFNE positron ring. The DAFNE simulations demonstrate that the modifications of the wiggler field enhance the electron cloud build up and that, on the other hand, the new beam parameters reduce it. The simulated electron densities in the wiggler are consistent with the observed tune shift for the old beam parameters. Both single- and multi-bunch instabilities can have rise times as low as the observed value of 10 μs. Simulations of the single-bunch instability in DAFNE exhibit a threshold in electron density which is of similar magnitude as both the simulated density and the one inferred from the measured tune shift. However, a single bunch instability would be expected to occur also in the vertical plane, whereas the stripe-like distribution of the electrons may favor horizontal multi-bunch instabilities.
Possible countermeasures against electron-cloud build up include clearing electrodes, grooved surfaces [22, 23], and optimized photon absorbers [24] or radiation masks with low reflectivity and low photoemission yield.
Electron-cloud effects will have to be considered at an early stage in the wiggler design for linear-collider damping rings.

Acknowledgements

This work is supported in part by the Commission of the European Communities under the 6th Framework Programme "Structuring the European Research Area", contract RIDS-011899.
We would like to thank R. Cimino for measuring surface parameters of the DAFNE vacuum chambers, as well as G. Bellodi, E. Benedetto, H. Braun, M. Furman, M. Korostelev, K. Ohmi, M. Pivi, P. Raimondi, and F. Ruggiero for their collaboration and for many helpful discussions. We also thank I. Wilson for a careful reading of the document.

References

[1] D. Schulte, R. Wanzenberg, F. Zimmermann, ECLOUD'04 Napa (2004).

[2] C. Vaccarezza, R. Cimino, A. Drago, M. Zobov, D. Schulte, F. Zimmermann, G. Rumolo, K. Ohmi, M. Pivi, "Electron Cloud Build-Up Study for DA*F*NE," PAC 2005 Knoxville (2005).

[3] F. Zimmermann, A. Rossi, "Synchrotron Radiation in the LHC Experimental Insertions," CERN-LHC-Project-Report-675 (2003).

[4] C. Vaccarezza, private communication (2005).

[5] G. Rumolo, F. Zimmermann, *Practical User Guide for ECloud*, CERN-SL-Note-2002-016 AP (2002).

[6] M. Pivi, private communication (2004); see also M. Woodley, A. Wolski, *The NLC Main Damping Ring Lattice*, LCC-0113, CBP Tech Note-276 (2003).

[7] M. Venturini, "Effect of Wiggler Insertions on the Single-Particle Dynamics of the NLC Main Damping Rings," LBNL-53264 (2003).

[8] M. Korostelev, 'Requirements and Studies for CLIC," WIGGLE'05 Frascati (2005).

[9] P. Vobly, "Magnetic Field Calculations and Design Optimization of the Wigglers for CLIC Damping Ring," WIGGLE'05 Frascati (2005).

[10] K. Ohmi, "Beam and Photoelectron Interactions in Positron Storage Rings," PRL 75, 1526 (1995).

[11] K. Ohmi, F. Zimmermann, "Head-Tail Instability Caused by Electron Cloud in Positron Storage Rings," PRL 85, 3821 (2000).

[12] K. Ohmi, F. Zimmermann, E. Perevedentsev, "Wake Field and Fast Head-Tail Instability Caused by an Electron Cloud," Phys. Rev. E65, 016502 (2002).

[13] G. Rumolo, F. Zimmermann, *Practical User Guide for HEADTAIL*, CERN-SL-Note-2002-036 AP (2002).

[14] C. Vaccarezza et al., "Experimental Observations and Electron-Cloud Simulations at DAFNE," ECLOUD'04 Napa (2004).

[15] K. Ohmi, S. Heifets, F. Zimmermann, "Study of Coherent Tune Shift Caused by Electron Cloud in Positron Storage Rings," APAC'01 Beijing (2001).

[16] A. Drago, M. Zobov, D. Teytelman, "Recent Observations on a Horizontal Instability in the DAFNE Positron Ring," PAC2005 Knoxville (2005).

[17] F. Zimmermann, "Review of Single-Bunch Instabilities Driven by an Electron Cloud," PRST-AB 7, 124801 (2004).

[18] M. Preger, "The Wiggler Transfer Matrix," DAFNE Technical Note L-34 (2003).

[19] F. Le Pimpec, F. King, R.E. Kirby, "Electron Conditioning of Technical Aluminium Surfaces: Effect on the Secondary Electron Yield," SLAC-PUB-10894 (2004).

[20] D. Schulte, G. Arduini, V. Baglin, J.M. Jimenez, F. Ruggiero, F. Zimmermann, "Electron Cloud Measurements in the SPS in 2004," PAC2005 Knoxville (2005).

[21] F. Ruggiero, G. Rumolo, F. Zimmermann, "Simulation of the Electron-Cloud Build Up and Its Consequences on Heat Load, Beam Stability and Diagnostics," Proc. ICAP 2000, Darmstadt; CERN-SL-2000-073 AP; and PRST-AB 2, 012801 (2001).

[22] A.A. Krasnov, "Molecular Pumping Properties of the LHC Arc Beam Pipe and Effective Secondary Emission from Cu Surface with Artificial Roughness," LHC-Project-Report-671 (2003).

[23] G.V. Stupakov and M. Pivi, "Suppression of the Effective SEY for a Grooved Metal Surface," Proceedings ECLOUD'04, Napa, California, CERN-2005-001 (2005).

[24] P. Bauer et al., "Synchrotron Radiation Issues in the VLHC," Proc. IEEE PAC 2001 Chicago (2001).